Simulating Cosmic Reionisation

Pawlik, A.H.

Cuius rei demonstrationem mirabilem sane detexi. Hanc marginis exiguitas non caperet.

Fermat, margin note in his copy of Arithmetica of Diophantus

CHAPTER 5

TRAPHIC in GADGET implementation and tests

Andreas H. Pawlik & Joop Schaye

This chapter contains material that has been published together with the material presented in the previous chapter, Chapter 4, in MNRAS 389 (2008), 651-677. It provides an updated and significantly extended version of Section 5 in that publication.

We present and test a parallel numerical implementation of our radiative transfer scheme TRAPHIC, specified for the transport of monochromatic hydrogen-ionising radiation, in the smoothed particle hydrodynamics code GADGET-2. The tests comprise several radiative transfer problems of increasing complexity. Some of these tests have been specifically designed to investigate TRAPHIC's ability to solve the radiative transfer problem in the large cosmological reionisation simulations that it was developed for, while others have been designed to demonstrate that TRAPHIC can also be employed in more general contexts. The results of all tests are in excellent agreement with both analytic solutions and numerical reference results obtained with state-of-the-art radiative transfer codes.

5.1 INTRODUCTION

Ionising radiation is thought to play a key role in determining the ionisation state and shaping the spatial distribution of the baryonic matter in our Universe on both small and large scales. Examples include the triggering and quenching of star formation through radiative feedback from nearby ionising stellar sources both in the early (e.g. Yoshida et al. 2007; Wise & Abel 2007; Johnson, Greif, & Bromm 2007; Alvarez, Bromm, & Shapiro 2006; Susa & Umemura 2006) and present-day universe (e.g. Gritschneder et al. 2007; Dale, Bonnell, & Whitworth 2007), the thin shell instability (for a recent simulation see Whalen & Norman 2007) and the growth and percolation of ionised regions generated by the first stars and quasars during the so-called Epoch of Reionisation (for recent simulations see e.g. Iliev et al. 2006a; Trac & Cen 2007; Kohler, Gnedin, & Hamilton 2007; Paschos et al. 2007). Accomplishing the transport of ionising radiation in hydrodynamical simulations of our Universe, both on large and small scales, in an efficient, computationally feasible manner has therefore become one of the primary goals in numerical astrophysics.

TRAPHIC is a novel radiative transfer scheme that we have developed to solve the radiative transfer problem in Smoothed Particle Hydrodynamics (SPH) simulations (Chapter 4). Its design has been guided by the wish to transport radiation in an adaptive manner directly on the unstructured grid traced out by the particles in SPH simulations, in parallel on distributed memory and with a computation time that does not scale with the number of radiation sources. This is done by transporting photon packets subject to absorption and scattering on a particle-by-particle basis with a well-defined spatial and angular resolution. In this chapter we apply TRAPHIC to the transport of ionising radiation.

It is helpful to briefly recall some basic concepts and notations that we have used in our description of TRAPHIC in Chapter 4 and that will be frequently employed here. The transport process can be decomposed into the emission of photon packets by source particles followed by their directed transport on the irregular set of SPH particles. Photon packets are emitted from source particles to their $\tilde{N}_{\mathrm{ngb}}$ neighbouring SPH particles (residing in a sphere of radius $\tilde{h}$ centred on the source) using a tessellating set of N_{c} emission cones. The number of cones is a parameter that determines the angular resolution of the radiative transfer. The number of neighbours $\tilde{N}_{\mathrm{ngb}}$ is a parameter that determines the spatial resolution and is usually matched to the number of neighbours N_{ngb} (residing in the sphere of radius h) used in the computation of the SPH particle properties, $\tilde{N}_{\mathrm{ngb}} \lesssim N_{\mathrm{ngb}}$.

To each of the emitted photon packets we associate a propagation direction that is parallel to the central axis of the corresponding emission cone. After emission, the photon packets are traced downstream along their propagation direction. The packets thereby remain confined to the solid angle they were originally emitted into thanks to the use of transmission cones with solid angle $4\pi/N_{\mathrm{c}}$. Virtual particles (ViPs) are introduced to accomplish the photon transport along directions for which no neighbouring SPH particle could be found in the associated cones. Finally, the photon transport is supplemented with a photon packet (or, equivalently, source) merging procedure that respects the chosen angular resolution to strictly limit the required computation time.

The photon transport is performed using (radiative transfer) time steps Δt_{r}. During each such time step, photons are propagated and their interactions with the gas are computed until a certain stopping criterion is satisfied. The form of this criterion depends on whether one aims to solve the time-independent or the time-dependent radiative transfer equation. In the first case, photons are propagated until they are absorbed or have left the computational domain. In the second case, photon clocks associated with each photon packet are used to synchronise

the packet's travel time with the simulation time such that the photon packet travels at the speed of light. After each time step, the state of the SPH particles is updated according to the interactions (absorptions, scatterings) with photon packets they experienced. Finally, the radiative transfer time is advanced, which concludes the algorithm. The reader is referred to Chapter 4 for more details.

This chapter is organised as follows. We start by briefly reviewing the physics of photo-ionisation (Sec. 5.2). We will then describe a numerical implementation of TRAPHIC specified for the transport of mono-chromatic hydrogen-ionising radiation in the SPH code GADGET-2 (Springel 2005) (Sec. 5.3). We will verify our implementation in several tests that are set up to allow comparisons to accurate reference solutions, obtained either analytically or numerically with state-of-the-art radiative transfer codes (Sec. 5.4). Finally, we will present our conclusions (Sec. 5.5).

5.2 PHOTO-IONISATION RATE EQUATION

Here we briefly recall the principles of the photo-ionisation and recombination process occurring for a hydrogen-only gas parcel of mass density ρ exposed to hydrogen-ionising radiation. We will employ the equations derived in this section in the description of the numerical implementation of TRAPHIC.

Hydrogen-ionising photons can be absorbed by neutral hydrogen. The absorption strength is typically expressed using the frequency-dependent mass absorption coefficient κ_ν for hydrogen-ionising radiation (e.g. Osterbrock 1989). For the demonstrational purpose of this chapter it will be sufficient to approximate the frequency-dependence of κ_ν by (see, e.g., Fig. 7.1 in Chapter 7)

$$\kappa_\nu \equiv \frac{\sigma_\nu n_{\rm HI}}{\rho} \tag{5.1}$$

$$\sigma_\nu = \sigma_0 \left(\frac{\nu}{\nu_0}\right)^{-3} \Theta(\nu-\nu_0), \tag{5.2}$$

with $n_{\rm HI} = (1-\chi)\rho/m_{\rm H}$ the neutral hydrogen number density, ν_0 the Lyman-limit frequency of energy $h_{\rm p}\nu_0 = 13.6$ eV, $\sigma_0 = 6.3 \times 10^{-18}$ cm^2 the absorption cross-section for photons at the Lyman-limit, $m_{\rm H}$ the mass of a hydrogen atom and $\Theta(x)$ the Heaviside step function; the ionised fraction is $\chi \equiv n_{\rm HII}/n_{\rm H}$. The number of photo-ionisations per unit time per neutral hydrogen atom at a certain point in space is determined by the photo-ionisation rate Γ,

$$\Gamma = \int_0^\infty d\nu \, \frac{4\pi J_\nu(\nu)}{h_{\rm p}\nu}\sigma_\nu, \tag{5.3}$$

where $J_\nu \equiv \int d\Omega \; I_\nu/(4\pi)$ is the mean ionising intensity. The rate of change of the neutral fraction $\eta \equiv 1-\chi$ at this point is then

$$\frac{d}{dt}\eta = \alpha(T) n_{\rm e} \chi - \Gamma\eta \equiv \frac{\chi}{\tau_{\rm rec}} - \frac{\eta}{\tau_{\rm ion}}. \tag{5.4}$$

In the last equation, $\alpha(T)n_{\rm e}$ is the number of recombinations occurring per unit time per ionised hydrogen atom, $\tau_{\rm rec} \equiv 1/(\alpha n_{\rm e})$ is the recombination time scale and $\tau_{\rm ion} \equiv 1/\gamma$ is the photo-ionisation time scale.[1]

[1]Note that in Eq. 5.4 collisional ionisations can easily be taken into account by replacing Γ with $(\Gamma + C(T)n_{\rm e})$,

With the definition $\tilde{\chi} \equiv \tau_{\rm rec}/(\tau_{\rm ion} + \tau_{\rm rec})$ we can rewrite Eq. 5.4 to read

$$\frac{d\chi}{dt} = -\frac{\chi - \tilde{\chi}}{\tau_{\rm ion}\tilde{\chi}}. \tag{5.5}$$

Setting $d\chi/dt = 0$ yields the equilibrium ionised fraction $\chi_{\rm eq} = \tau_{rec,eq}/(\tau_{\rm ion} + \tau_{rec,eq})$. Over time scales that are short compared with $\tau_{\rm rec}/|d\tau_{\rm rec}/dt|$ and $n_{\rm e}/|dn_{\rm e}/dt|$, Eq. 5.5 constitutes a first order linear homogeneous differential equation in $\chi - \tilde{\chi}$ with constant coefficients, whose solution reads

$$\chi(t) - \chi_{\rm eq} = (\chi(t_0) - \chi_{\rm eq})e^{-\frac{t-t_0}{\tau_{\rm eq}}} \tag{5.6}$$

$$\tau_{\rm eq} \equiv \frac{\tau_{\rm ion}\tau_{\rm rec}}{\tau_{\rm ion} + \tau_{\rm rec}}. \tag{5.7}$$

From Eq. 5.6 we see that the equilibrium ionised fraction is exponentially approached on the instantaneous ionisation equilibrium time scale $\tau_{\rm eq}$. We will employ this time scale later on for the numerical integration of the rate equation.

We emphasise that our derivation of Eq. 5.6 was based on the assumption that the electron density does not change significantly. We have adopted this assumption in order to point out the characteristic time scales involved. In Sec. 5.4.1 we will present an alternative derivation of the solution of the photo-ionisation rate equation (Eq. 5.4) that is also valid for the case of an evolving electron density.

5.3 NUMERICAL IMPLEMENTATION

We have adapted the description of TRAPHIC that we have presented in Chapter 4 for the transport of hydrogen-ionising radiation according to the physics of photo-ionisation as reviewed in Sec. 5.2. We implemented it using a single frequency bin in the parallel N-body-Tree-SPH code GADGET-2 (Springel 2005). The description of (important aspects of) this implementation is the subject of this section.

5.3.1 Transport of ionising photons and computation of the photo-ionisation rate

The transport of ionising photons is performed in finite radiative transfer time steps of size $\Delta t_{\rm r}$, during which photon packets emitted by ionising sources are propagated through the SPH density field guided by cones as we have described in Chapter 4. This propagation starts with the emission of photons using a set of tessellating emission cones with random orientation. For definiteness, we present our choice of the emission cone tessellation in App. 5.B.1 and our implementation of the random rotations applied to it in App. 5.B.2.

During each time step the number of photons that are absorbed by neutral hydrogen is computed using the absorption coefficient κ_ν, given by Eqs. 5.1 and 5.2, together with the expression for the optical depth in Chapter 4 (Eq. 4.10). At the end of the time step, i.e. at time $t_{\rm r} + \Delta t_{\rm r}$, where $t_{\rm r}$ is the simulation time, the number of ionising photons $\Delta\mathcal{N}_{{\rm in},i}$ impinging on and the number of ionising photons $\Delta\mathcal{N}_{{\rm abs},i}$ absorbed by particle i over the time interval $\Delta t_{\rm r}$

where $C(T)n_{\rm e}$ describes the number of collisional ionisations per unit time per neutral hydrogen atom. In this chapter, however, we assume that collisional ionisations are unimportant, setting $C \equiv 0$ throughout. We will extend our description to include collisional ionisations in Chapter 7.

are then known. The photo-ionisation rate Γ_i is obtained directly from the number of absorbed photons using

$$\eta_i^{t_\mathrm{r}} \mathcal{N}_{\mathrm{H},i} \Gamma_i^{t_\mathrm{r}} \Delta t_\mathrm{r} \;=\; \Delta\mathcal{N}_{\mathrm{in},i} \left[1 - \exp(-\tau_i^{t_\mathrm{r}})\right], \tag{5.8}$$

where $\mathcal{N}_{\mathrm{H},i} \equiv m_i^{t_\mathrm{r}} X_i^{t_\mathrm{r}} / m_\mathrm{H}$ is the number of hydrogen atoms associated with particle i (X_i is the hydrogen mass fraction) and superscripts indicate the time at which quantities are evaluated. Thereby

$$\tau_i^{t_\mathrm{r}} \equiv -\ln\left(1 - \frac{\Delta\mathcal{N}_{\mathrm{abs},i}}{\Delta\mathcal{N}_{\mathrm{in},i}}\right) \tag{5.9}$$

is the a posteriori optical depth[2] that relates the number of impinging photons $\Delta\mathcal{N}_{\mathrm{in},i}$ to the number of absorbed photons $\Delta\mathcal{N}_{\mathrm{abs},i}$. In the next section we describe how the photo-ionisation rate is used to update the neutral fraction of particle i.

5.3.2 Solving the rate equation

The photo-ionisation rate equation, i.e. the differential equation Eq. 5.4, belongs to a class of problems that are referred to as stiff (for useful introductions to stiff problems see, e.g., Shampine & Gear 1979; Press et al. 1992). There is no universally accepted definition of stiffness. Often, the classification of a problem as stiff is based on examinations of the stability of numerical integrators applied to solve this problem.

As an example, consider the equation (cp. Press et al. 1992)

$$\frac{d}{dt} y = -\frac{y}{\tau} \tag{5.10}$$

with solution

$$y(t) = y(t_0) e^{-(t-t_0)/\tau} \tag{5.11}$$

Hereby, τ is a constant with dimensions of time. Accordingly, the equilibrium solution obtained considering the limit $t \to \infty$ is $y \to 0$. The explicit (or forward) Euler scheme for integrating this equation with step size Δt is (Press et al. 1992)

$$y^{t+\Delta t} = y^t + \Delta t \frac{d}{dt} y^t = y^t (1 - \frac{\Delta t}{\tau}), \tag{5.12}$$

where we used Eq. 5.10 in the last step. The method is unstable for $\Delta t/\tau > 2$ as then $|y| \to \infty$ for $t \to \infty$. Its stable integration requires steps $\Delta t < 2\tau$, which become prohibitively small for $\tau \to 0$. Observe that this limit on the integration step is independent of the value of the solution y. Small integration steps are therefore needed even when simulating the equilibrium solution, despite the fact that this solution is not changing at all.

Applied to the integration of the photo-ionisation rate equation (Eq. 5.4), the explicit Euler scheme reads

$$\frac{\eta_i^{t_\mathrm{r}+\Delta t_\mathrm{r}} - \eta_i^{t_\mathrm{r}}}{\Delta t_\mathrm{r}} = \alpha_i^{t_\mathrm{r}} n_{\mathrm{e},i}^{t_\mathrm{r}} \chi_i^{t_\mathrm{r}} - \Gamma_i^{t_\mathrm{r}} \eta_i^{t_\mathrm{r}} \tag{5.13}$$

In Appendix 5.A we demonstrate that in order not to violate the physical bound $0 \leq \eta_i \leq 1$, the integration in the explicit Euler discretisation would require time steps $\Delta t_\mathrm{r} < \tau_\mathrm{eq}$, where τ_eq

[2]We use the expression *a posteriori* since this optical depth is computed *after* finishing the transport of photons over the radiative transfer time step Δt_r, using the *total* number of photons $\Delta\mathcal{N}_{\mathrm{in},i}$ and $\Delta\mathcal{N}_{\mathrm{abs},i}$ that were, respectively, impinging on and absorbed by particle i over that time step.

is the characteristic time scale over which the neutral fraction changes (see Eq. 5.7). We would like to choose the radiative transfer time step Δt_r independently of the time scale τ_eq because the latter can be prohibitively small to allow efficient radiative transfer computations. In the following, we discuss two approaches to accomplish this.

Implicit integration

The first approach to decouple the radiative transfer time step Δt_r from the time scale τ_eq we consider is the use of implicit integrators. These integrators, which advance the solution based on the advanced solution itself, are in fact commonly employed to deal with stiff problems like the problem at hand. As an example, consider the so-called implicit or (backward) Euler integration of Eq. 5.10 (Press et al. 1992),

$$y^{t+\Delta t} = y^t + \Delta t \frac{d}{dt} y^{t+\Delta t} = y_t + \Delta t(-\frac{y^{t+\Delta t}}{\tau}), \tag{5.14}$$

or,

$$y^{t+\Delta t} = \frac{y^t}{1+\Delta t/\tau}. \tag{5.15}$$

This integrator is stable: even for $\Delta t \to \infty$ it yields $y \to 0$ as $t \to \infty$, which is the correct equilibrium solution. Note, however, that this gain in stability typically comes along with a loss in accuracy in following the approach to equilibrium (Press et al. 1992).

Applied to the integration of the photo-ionisation rate equation, Eq. 5.4, the backwards Euler scheme reads

$$\frac{\eta_i^{t_\mathrm{r}+\Delta t_\mathrm{r}} - \eta_i^{t_\mathrm{r}}}{\Delta t_\mathrm{r}} = \alpha_i^{t_\mathrm{r}+\Delta t_\mathrm{r}} n_{\mathrm{e},i}^{t_\mathrm{r}+\Delta t_\mathrm{r}} \chi_i^{t_\mathrm{r}+\Delta t_\mathrm{r}} - \Gamma_i^{t_\mathrm{r}+\Delta t_\mathrm{r}} \eta_i^{t_\mathrm{r}+\Delta t_\mathrm{r}}. \tag{5.16}$$

To proceed, we need to evaluate the photo-ionisation rate $\Gamma_i^{t_\mathrm{r}+\Delta t_\mathrm{r}}$ at time $t_\mathrm{r}+\Delta t_\mathrm{r}$. Because of the discretisation of the photon transport using times steps Δt_r, the flux $d\mathcal{N}_{\mathrm{in},i}/dt$ of ionising photons impinging on particle i may be considered as constant over the time step Δt_r, i.e. $d\mathcal{N}_{\mathrm{in},i}/dt = \Delta\mathcal{N}_{\mathrm{in},i}/\Delta t_\mathrm{r}$. Employing the last equality in Eq. 5.8 yields the following, instantaneous scaling of the photo-ionisation rate,

$$\Gamma(\eta) \propto (1 - e^{-\tau(\eta)})\eta^{-1}. \tag{5.17}$$

A similar derivation of this scaling can be found in Mellema et al. (2006). Hence,

$$\Gamma_i^{t_\mathrm{r}+\Delta t_\mathrm{r}} = \Gamma_i^{t_\mathrm{r}} \left[\frac{1-\exp(-\tau_i^{t_\mathrm{r}+\Delta t_\mathrm{r}})}{1-\exp(-\tau_i^{t_\mathrm{r}})}\right] \frac{\eta_i^{t_\mathrm{r}}}{\eta_i^{t_\mathrm{r}+\Delta t_\mathrm{r}}}, \tag{5.18}$$

where $\Gamma_i^{t_\mathrm{r}}$ and $\tau_i^{t_\mathrm{r}}$ are the photo-ionisation rate and the optical depth at the beginning of the step, given by Eqs. 5.8 and 5.9, and $\tau_i^{t_\mathrm{r}+\Delta t_\mathrm{r}} = \tau_i^{t_\mathrm{r}} \eta_i^{t_\mathrm{r}+\Delta t_\mathrm{r}}/\eta_i^{t_\mathrm{r}}$ is the optical depth at time $t_\mathrm{r}+\Delta t_\mathrm{r}$.

In general, Eq. 5.16 needs to be solved iteratively[3]. This may be done by finding the zero of the function

$$f(\chi_i^{t_\mathrm{r}+\Delta t_\mathrm{r}}) = \frac{\chi_i^{t_\mathrm{r}+\Delta t_\mathrm{r}} - \chi_i^{t_\mathrm{r}}}{\Delta t_\mathrm{r}} + \alpha_i^{t_\mathrm{r}+\Delta t_\mathrm{r}} n_{\mathrm{e},i}^{t_\mathrm{r}+\Delta t_\mathrm{r}} \chi_i^{t_\mathrm{r}+\Delta t_\mathrm{r}} - \Gamma_i^{t_\mathrm{r}+\Delta t_\mathrm{r}}(1-\chi_i^{t_\mathrm{r}+\Delta t_\mathrm{r}}) \tag{5.19}$$

[3]For the special case $\eta = 1-\chi$ and a non-evolving photo-ionisation rate $\Gamma(\eta) = const$, Eq. 5.16 yields a quadratic equation that can be directly solved (Petkova & Springel 2008).

using a combination of bracketing (Press et al. 1992; to set the interval within which to look for the zero) and bisection (Press et al. 1992; to locate the zero).

Because the neutral fraction changes continuously within the time step (although this is hidden behind the implicit integrator), the number of ionisations $\Delta\mathcal{N}_{\mathrm{impl},i}$ that have been used to advance it may be less than the number of photons $\Delta\mathcal{N}_{\mathrm{abs},i}$ that have been removed due to absorptions during the radiation transport over the time step Δt_{r} based on the assumption of a non-evolving neutral fraction. Photon conservation requires reinserting the number of absorbed photons that have not been used to advance the ionised fraction, $\Delta\mathcal{N}_{\mathrm{abs},i}^{t_{\mathrm{r}}} - \Delta\mathcal{N}_{\mathrm{impl},i}^{t_{\mathrm{r}}}$, into the photon transport (in the next radiative transfer time step). This number is, however, not well-defined, because the decomposition of the change in the ionised fraction as being due to ionisations or recombinations is ambiguous.

A possible interpretation of Eq. 5.16 is that the first term on the right-hand side determines the number of recombinations, while the second term determines the number of ionisations that have led to the change $\eta_i^{t_{\mathrm{r}}+\Delta t_{\mathrm{r}}} - \eta_i^{t_{\mathrm{r}}}$ of the neutral fraction over the time step Δt_{r}. If we follow this interpretation, we find that the number of ionising photons that have been used to advance the neutral fraction is

$$\Delta\mathcal{N}_{\mathrm{impl},i}^{t_{\mathrm{r}}} = \mathcal{N}_{\mathrm{H},i}^{t_{\mathrm{r}}}\Gamma_i^{t_{\mathrm{r}}+\Delta t_{\mathrm{r}}}\eta_i^{t_{\mathrm{r}}+\Delta t_{\mathrm{r}}}\Delta t_{\mathrm{r}}. \tag{5.20}$$

Note, however, that this interpretation of Eq. 5.16 is only one of (infinitely) many interpretations. This ambiguity makes it generally impossible to strictly conserve photons when employing the implicit Euler integrator.

The loss of accuracy during the approach to equilibrium and the impossibility of a strictly photon-conserving formulation lead us to consider a more direct integration method that does not suffer from these problems.

Explicit integration: Sub-cycling

To decouple the radiative transfer time step Δt_{r} from the time scale τ_{eq} in a strictly photon-conserving manner, we employ the following sub-cycling procedure. We explicitly follow the evolution of the neutral fraction during the time interval $t_{\mathrm{r}} \leq t_i < t_{\mathrm{r}} + \Delta t_{\mathrm{r}}$ on sub-cycle steps $\delta t_i \leq \Delta t_{\mathrm{r}}$,

$$\eta_i^{t_i+\delta t_i} - \eta_i^{t_i} = \alpha_i^{t_i} n_{\mathrm{e},i}^{t_i}\chi_i^{t_i}\delta t_i - \Gamma_i^{t_i}\eta_i^{t_i}\delta t_i. \tag{5.21}$$

As noted above (Eq. 5.17), the photo-ionisation rate $\Gamma(\eta) \propto (1 - e^{-\tau(\eta)})\eta^{-1}$. Hence, a change in the neutral fraction implies a change in the photo-ionisation rate $\Gamma_i^{t_i}$,

$$\Gamma_i^{t_i} = \Gamma_i^{t_{\mathrm{r}}}\left[\frac{1-\exp(-\tau_i^{t_i})}{1-\exp(-\tau_i^{t_{\mathrm{r}}})}\right]\frac{\eta_i^{t_{\mathrm{r}}}}{\eta_i^{t_i}}, \tag{5.22}$$

where $\Gamma_i^{t_{\mathrm{r}}}$ and $\tau_i^{t_{\mathrm{r}}}$ are the photo-ionisation rate and the optical depth at the beginning of the sub-cycling, given by Eqs. 5.8 and 5.9, and $\tau_i^{t_i} = \tau_i^{t_{\mathrm{r}}}\eta_i^{t_i}/\eta_i^{t_{\mathrm{r}}}$ is the optical depth at time t_i.

The number of ionisations $\Delta\mathcal{N}_{\mathrm{sub},i}$ occurring over the radiative transfer time step Δt_{r} is then $\Delta\mathcal{N}_{\mathrm{sub},i} = \mathcal{N}_{\mathrm{H},i}\sum\Gamma_i^{t_i}\eta_i^{t_i}\delta t_i$, where the sum is over all sub-steps δt_i in $(t_{\mathrm{r}}, t_{\mathrm{r}} + \Delta t_{\mathrm{r}})$. We set $\delta t_i \equiv \min(f\tau_{\mathrm{eq},i}^{t_i}, t_{\mathrm{r}} + \Delta t_{\mathrm{r}} - t_i)$, where $f < 1$ is a dimensionless factor. That is, we follow the evolution of the neutral fraction using an integration step that ensures its accurate integration (see Appendix 5.A). If $\Delta\mathcal{N}_{\mathrm{sub},i} = \Delta\mathcal{N}_{\mathrm{abs},i}$ for $t_i < t_{\mathrm{r}} + \Delta t_{\mathrm{r}}$, we set $\Gamma_i^{t_i} = 0$ for the remaining

sub-cycles[4]. If at the end of the sub-cycling $\Delta\mathcal{N}_{\mathrm{sub},i} < \Delta\mathcal{N}_{\mathrm{abs},i}$, we explicitly conserve photons by adding $\Delta\mathcal{N}_{\mathrm{abs},i} - \Delta\mathcal{N}_{\mathrm{sub},i}$ photons to the photon transport in the next radiative transfer step.

When either the photo-ionisation rate or the recombination rate is high, τ_{eq} and hence δt will be very small (dropping the particle index i for simplicity). For $\delta t \ll \Delta t_{\mathrm{r}}$ the sub-cycling would become computationally very expensive. We could set a lower limit to the sub-cycling step δt to speed up the numerical integration of the rate equation. Of course, this would imply a loss of accuracy, and until the physical problem would re-adjust to match the condition $\delta t < \tau_{\mathrm{eq}}$, the numerical integration could even lead to a neutral fraction outside the physical range $0 \leq \eta \leq 1$. For instance, the number of ionisations $\Delta\mathcal{N}_{\mathrm{sub}}$ occurring for a particle during the sub-cycling over the time step Δt_{r} could then be larger than the number of neutral atoms $\eta^{t_{\mathrm{r}}}\mathcal{N}_{\mathrm{H}}^{t_{\mathrm{r}}}$ it represents at the beginning of the time step. In this case we could set $\eta = 0$ and add $\Delta\mathcal{N}_{\mathrm{sub}} - \eta^{t_{\mathrm{r}}}\mathcal{N}_{\mathrm{H}}^{t_{\mathrm{r}}}$ photons to the photon transport in the next radiative transfer time step.

We find, however, that photo-ionisation equilibrium is typically reached after only a few sub-cycles. Once photo-ionisation equilibrium is reached, integration of the rate equation is no longer necessary, since the solution does not change anymore. Instead of imposing a minimum size on the sub-cycle step, we therefore take the following short-cut to speed up the computation. We integrate the rate equation over the few sub-cycles required to reach equilibrium. Thereafter, we stop and simply keep the neutral fraction fixed. As opposed to imposing a minimum size on the sub-cycle step, this approach gives the exact solution. At the same time, it is very fast. For a photon-conserving transport we still need to know the number of photo-ionisations and recombinations occurring during the equilibrium phase. Both can, however, be obtained in a stroke, based on the number of photo-ionisations and recombinations that occurred during the last sub-cycle step over which the rate equation was integrated explicitly.

An evolving photo-ionisation rate

In the above presentation of our numerical implementation of the integration of the photo-ionisation rate equation we have changed the photo-ionisation rate according to the changes in the neutral fraction during that integration (Eq. 5.22). The importance[5] of properly following the evolution of the photo-ionisation rate in the presence of an evolving neutral fraction has been pointed out by Mellema et al. (2006). There, a time-averaged photo-ionisation rate obtained from an iterative (implicit) procedure was employed. While the derivation of the Mellema et al. (2006) procedure assumes a vanishing recombination rate (see the discussion in their Sec. 2.2), the sub-cycling procedure (Eq. 5.22) presented here does not suffer from this limitation.

If one is only interested in obtaining the equilibrium neutral fraction, the detailed handling of the photo-ionisation rate is, however, rather unimportant. This is because ionisation equilibrium implies that the number of photo-ionisations $d\mathcal{N}_{\mathrm{in}}/dt(1-e^{-\tau})\Delta t_{\mathrm{r}}$ over the time interval Δt_{r} exactly equals the number of recombinations $(1-\eta)\mathcal{N}_{\mathrm{H}} n_{\mathrm{e}} \alpha \Delta t_{\mathrm{r}}$ over that same time interval.

[4]The particle then only recombines. This situation essentially occurs because the radiative transfer is discretized using finite time steps. In reality (i.e. for time steps $\Delta t_{\mathrm{r}} \rightarrow 0$), the ionisation rate will be constant. One may therefore also consider not to change the photo-ionisation rate, even though all photons that have been absorbed over the time step have already been used up in the integration of the photo-ionisation rate equation, to prevent the particle from artificially recombining.

[5]As already pointed out by Mellema et al. (2006), it actually is only important for large optical depths. For $\tau \ll 1$, Eq. 5.22 implies that the photo-ionisation rate is constant, $\Gamma_i^{t_i} = \Gamma_i^{t_{\mathrm{r}}}$. In the optically thick regime, the assumption of $\Gamma = const$ would, however, generally lead to an underestimate of the true photo-ionisation rate, since $\Gamma(\eta) \propto (1-e^{-\tau(\eta)})\eta^{-1}$ is a monotonically increasing function of decreasing neutral fraction (see Fig. 1 in Mellema et al. 2006).

This balance, however, has a unique (and stable; see Eq. 5.6) solution for the neutral fraction[6]. The equilibrium neutral fraction then also implies the correct photo-ionisation rate, via Eq. 5.8. When one is interested in following the details of the evolution of the neutral fraction towards photo-ionisation equilibrium, on the other hand, the dependence of the photo-ionisation rate on the neutral fraction needs to be taken into account, as presented above.

5.3.3 The time step $\Delta t_{\rm r}$

Our main consideration when choosing the size of the radiative transfer time step for the simulations we are presenting in this work, is that we wish to accurately reproduce the analytical and numerical reference results we are comparing with. These results include the time-dependence of the size of ionised regions around ionising sources. At early times, just after the sources start to emit ionising photons, the ionised regions expand quickly into the neutral hydrogen field surrounding the sources. To accurately reproduce this early phase of rapid growth, we necessarily have to employ time steps $\Delta t_{\rm r}$ that are relatively small. The phase of rapid growth is, however, only of relatively short duration. The subsequent evolutionary stages of modest resp. slow growth, which account for most of the (simulation) time, are often more interesting. We show in Sec. 5.4.2 that whenever we are not interested in the very early phase of rapid growth we can, thanks to the photon-conserving nature of TRAPHIC, choose substantially larger time steps without affecting the final outcome of our simulations.

For all but one of the simulations we present in this work, we will be concerned with solving the time-independent radiative transfer equation (see Sec. 4.4.4 in Chapter 4). In these simulations, we choose to propagate photon packets downstream from their location of emission only over a single inter-particle distance per radiative transfer time step, unless stated otherwise. This approach is equivalent to solving the time-independent radiative transfer equation in the limit of small radiative transfer time steps[7], $\Delta t_{\rm r} \rightarrow 0$. We have explicitly checked for all our simulations that the time step was chosen sufficiently small to be in agreement with this limit.

Our treatment of the time-independent radiation transport reduces the computational effort for the simulation of problems for which the time step has been fixed to a small value, e.g. by considerations like those presented in the beginning of this section. In the limit that radiation completely fills the simulation box, the computational effort required to solve the time-independent radiative transfer equation over the time interval T by propagating photon packets only over a single inter-particle distance per radiative transfer time step $\Delta t_{\rm r}$ is proportional to (cp. Sec. 4.4.2) $N_{\rm SPH} \times \tilde{N}_{\rm ngb} \times N_{\rm c} \times T/\Delta t_{\rm r}$. This has to be compared to the computational effort required to follow all photon packets over each time step until they leave the simulation box, which is proportional to $N_{\rm SPH} \times \tilde{N}_{\rm ngb} \times N_{\rm c} \times N_{\rm SPH}^{1/3} \times T/\Delta t_{\rm r}$. This is larger by a factor of $N_{\rm SPH}^{1/3}$, which for typical simulations reaches values of the order of 100.

In Sec. 5.4.5 we will present one simulation in which we solve the time-dependent radiative transfer equation. In this simulation we will employ the photon clock (see Chapter 4) to accurately control the distance over which photon packets are propagated over each time step $\Delta t_{\rm r}$ to match the light crossing distance $c\Delta t_{\rm r}$. In this context it is interesting to note that in the case of small time steps, i.e. $c\Delta t_{\rm r} < L_{\rm box}$, it is less expensive to solve the time-

[6] Note that this balance does not depend on the size of the time step $\Delta t_{\rm r}$, since it appears on both sides of the equation describing it.

[7] In the limit of small time steps $\Delta t_{\rm r} \rightarrow 0$, the time it takes for photons to travel to the simulation box boundaries by only propagating a single inter-particle distance per time step goes to zero. Hence, in this limit photons immediately leave the simulation box, as required for solving the time-independent radiative transfer equation.

dependent than the time-independent radiative transfer equation. This is because the computational effort to solve the time-dependent equation (again in the limit that radiation completely fills the simulation box and assuming that its boundaries are photon-absorbing) scales as $N_{\rm SPH} \times \tilde{N}_{\rm ngb} \times N_{\rm c} \times c\Delta t_{\rm r}/L_{\rm box} \times N_{\rm SPH}^{1/3} \times T/\Delta t_{\rm r}$, which is smaller than the computational effort for obtaining the time-independent solution (assuming that over each radiative transfer time step photon packets are transported until they leave the box) by the factor[8] $c\Delta t_{\rm r}/L_{\rm box}$.

5.3.4 Resampling

For some of the simulations that we present in Secs. 5.4.2 - 5.4.5 we employ the resampling technique described in Chapter 4 to reduce numerical artefacts that arise from the representation of the continuous density field with a discrete set of particles. The resampling requires the sampling of the SPH kernel used in GADGET-2, which is the spline given in Chapter 4, Eq. 4.4. We approximate this kernel by a Gaussian,

$$W_\sigma(r) = \frac{1}{(2\pi)^{3/2}\sigma^3}\exp(-r^2/2\sigma^2). \tag{5.23}$$

We find that with a standard deviation of $\sigma \sim 0.29 \times h$, the Gaussian provides a reasonable fit to the spline. A similar relation was employed in Alvarez, Bromm, & Shapiro (2006). When we resample the SPH density field, all SPH particles are redistributed by randomly displacing them from the positions given by the hydrodynamical simulation, with the probability to find a given particle displaced by the distance r given by Eq. 5.23. The (rare) displacements larger than h are discarded; in this case the original particle positions as determined by the hydrodynamical simulation are used.

5.3.5 Effective multi-frequency description - grey approximation

In our current implementation we use only a single frequency. Thus, we either assume that the ionising radiation is mono-chromatic, or we assume ionising radiation with a frequency spectrum J_ν and provide an effective multi-frequency description using only a single frequency bin. This is called the grey approximation (for a textbook discussion on the numerical treatment of multi-frequency radiation and the grey approximation see, e.g., Mihalas & Weibel Mihalas 1984).

For the latter case, we define a frequency-independent (grey) photo-ionisation cross-section $\bar{\sigma}$ such that the total photo-ionisation rate (Eq. 5.3) is conserved,

$$\Gamma = \int_0^\infty d\nu\, \frac{4\pi J_\nu(\nu)}{h_{\rm p}\nu}\sigma_\nu \equiv \bar{\sigma}\int_{\nu_0}^\infty d\nu\, \frac{4\pi J_\nu(\nu)}{h_{\rm p}\nu}, \tag{5.24}$$

with

$$\bar{\sigma} = \int_0^\infty d\nu\, \frac{4\pi J_\nu(\nu)}{h_{\rm p}\nu}\sigma_\nu \times \left[\int_{\nu_0}^\infty d\nu\, \frac{4\pi J_\nu(\nu)}{h_{\rm p}\nu}\right]^{-1}. \tag{5.25}$$

[8] Observe that for larger time steps, i.e. $\Delta t_{\rm r} \geq L_{\rm box}/c$, and assuming photon-absorbing boundaries, the computational effort for solving the time-dependent radiative transfer equation equals the computational effort for solving the time-independent radiative transfer equation. It exceeds the computational effort for solving the time-independent radiative transfer equation with photon packets propagating only a single inter-particle distance per radiative transfer time step if $c\Delta t_{\rm r} > L_{\rm box}/N_{\rm SPH}^{1/3}$.

We note that for the purpose of computing the photo-ionisation rate the grey approximation provides an exact description of the multi-frequency problem if the radiation spectrum $J_\nu(\nu)$ is known. If instead the radiation spectrum is also computed in the grey approximation, i.e. by performing radiative transfer simulations using only a single frequency bin, then this approximation will provide an exact description of the multi-frequency problem only in the optically thin regime. In the optically thick regime, the frequency dependence of the photo-ionisation cross-section results in a deformation of the radiation field spectral shape that favours high-energy photons, because low-frequency photons are more likely to be absorbed (Eq. 5.2). This *spectral hardening* can only be accounted for by performing true multi-frequency radiative transfer, i.e. by using sufficiently many frequency bins (see Sec. 7.6.2 in Chapter 7 for a discussion of spectral hardening).

In the following we will be interested in the special case where the mean intensity obeys a black-body spectrum with temperature $T_{\rm bb} = 10^5$ K. That is, $J_\nu(\nu) \propto B_\nu(\nu)$, where

$$B_\nu(\nu, T_{\rm bb}) = \frac{2h_{\rm p}}{c^2} \frac{\nu^3}{\exp\left(\frac{h_{\rm p}\nu}{kT_{\rm bb}}\right) - 1}, \tag{5.26}$$

is the Planck function. Eq. 5.25 then implies a value

$$\bar{\sigma} = 1.49 \times 10^{-18}\ {\rm cm}^{-2} \tag{5.27}$$

for the grey photo-ionisation cross-section.

5.4 TESTS

In this section we report the performance of the implementation of TRAPHIC that we have presented in the previous section in well-defined tests. We will demonstrate that TRAPHIC can be used to accurately solve the radiative transfer equation for hydrogen-ionising radiation in arbitrary geometries and arbitrary optical depth regimes.

We start by verifying the accuracy of our sub-cycling approach in computing the non-equilibrium neutral fraction (Sec. 5.4.1). We then perform several three-dimensional radiative transfer simulations of increasing complexity. These simulations comprise the evolution of the ionised region around a single star in a homogeneous density field (Sec. 5.4.2), the casting of a shadow behind an opaque obstacle (Sec. 5.4.1), the propagation of an ionisation front around a star in a centrally peaked density profile (Sec. 5.4.4) and the propagation of ionisation fronts driven by the ionising radiation of multiple stars in an inhomogeneous density field obtained from a cosmological simulation (Sec. 5.4.5).

We compare the results obtained with TRAPHIC with analytic solutions, where available. For all but the simplest test problems, however, no analytic solution is known, mainly due to the complex geometries involved. We have therefore designed the test problems in Secs. 5.4.1, 5.4.2 and 5.4.5 to closely follow the description given in the Cosmological Radiative Transfer Codes Comparison Project (Iliev et al. 2006b), which provides a useful set of numerical reference solutions to compare with. We have designed the test problems in Sec. 5.4.3 and 5.4.4 to resemble the corresponding test problems presented in Mellema et al. (2006). In addition, we have developed a radiative transfer code that solves the radiative transfer equation for spherically symmetric problems on a one-dimensional regular mesh. We refer to this code as TT1D (TestTraphic1D). We will use TT1D to obtain reference solutions for the spherically symmetric

test problems in Secs. 5.4.2 and 5.4.4. We will refer to these reference solutions as the exact solutions to the corresponding radiative transfer problems.

Throughout we will assume that the density field is static. We defer a discussion of radiative transfer simulations on dynamically evolving density fields to Chapter 6. To facilitate a direct comparison with Iliev et al. (2006b), we present results after mapping physical quantities defined on the SPH particles to a regular grid, unless stated otherwise. This is done using a mass-conserving SPH interpolation similar to the one described in Alvarez, Bromm, & Shapiro (2006) that we have implemented for this purpose. We opted for the SPH interpolation since it is consistent with the SPH simulation we are employing. For comparison, we repeated our analysis using TSC mass-conserving interpolation (Hockney & Eastwood 1988) but found no significant differences.

For all tests reported in this section we employ the on-the-spot approximation (e.g. Osterbrock 1989) in order to allow a direct comparison with Iliev et al. (2006b). In the on-the-spot approximation diffuse photons emitted during recombinations to the hydrogen ground energy level are assumed to be immediately re-absorbed by neutral hydrogen atoms close to the location of emission. The effect of recombination radiation can then be simply taken into account by setting the recombination coefficient α to the so-called case B value $\alpha_{\rm B}$, which can be well approximated by (see, e.g., Fig. 7.3 in Chapter 7)

$$\alpha_{\rm B}(T) = 2.59 \times 10^{-13} \left(\frac{T}{10^4 \, {\rm K}} \right)^{-0.7} \, {\rm cm}^3 \, {\rm s}^{-1}, \tag{5.28}$$

where $T \approx 10^4$ K is the gas temperature. We will report on the study of diffuse radiation in which we will explicitly follow the scattering of recombination photons instead of employing the on-the-spot approximation in future work.

To keep the tests problems clean, we furthermore assume that the gas temperature T is constant, taking $T = 10^4$ K for the ionised gas. In Chapter 7 we will extend our implementation of TRAPHIC to also compute the temperature of the gas, in a self-consistent manner in step with the evolution of its ionisation state, and repeat some of the test problems discussed here.

In their simulations, Iliev et al. (2006b) and Mellema et al. (2006) assumed that the speed of light is infinite, i.e. they solved the time-independent radiative transfer equation. For the comparison with these simulations we will therefore make the same assumption (recall Sec. 5.3.3 for the discussion of how we solve the time-independent radiative transfer equation). From now on, when referring to the radiative transfer equation, we therefore assume it to be of the time-independent form, unless stated otherwise. We will repeat one of the simulations presented in Sec. 5.4.5 to solve the time-dependent radiative transfer equation by employing the photon packet clocks as described in Sec. 4.4.4 in Chapter 4.

Since its publication in Pawlik & Schaye (2008), TRAPHIC has been continuously improved. An important change with respect to the description in Pawlik & Schaye (2008) is a new treatment of how virtual particles (ViPs) distribute the photons they absorbed amongst their $\tilde{N}_{\rm ngb}$ neighbouring SPH particles that have been used to compute the ViPs' neutral density. Previously, this was done by giving, to each of the neighbours, a fraction of the absorbed photons that is proportional to the value of the ViPs' SPH kernel at their position. In the current version, the distribution is done by giving, to each of the neighbours, a fraction of the absorbed photons that is proportional to the neutral mass with which they contributed to the SPH estimate of the neutral density of the given ViP. The new way of distributing the absorptions is more consistent, since each of the SPH neighbours contributed to the ViP's absorptions coefficient (that is then used to compute the number of photons it absorbs and distributes amongst its

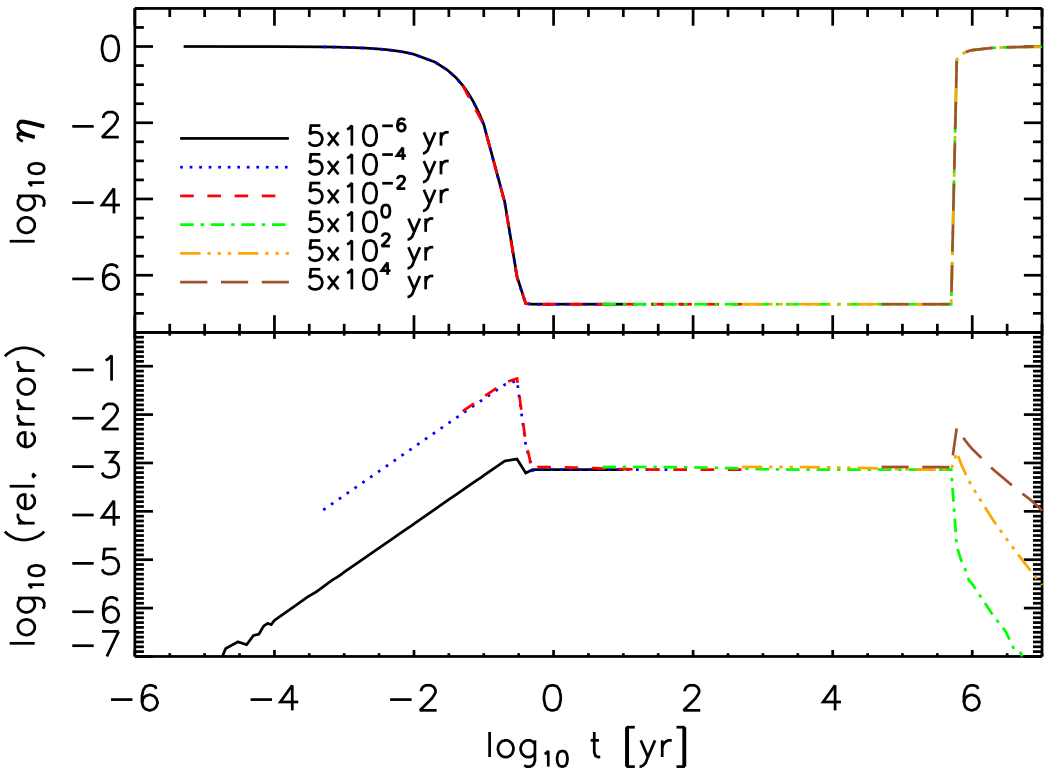

Figure 5.1: Test 0. Optically thin gas particle ionising up and recombining. *Top panel:* evolution of the neutral fraction obtained from the numerical integration (using Euler sub-cycling) of the photo-ionisation rate equation (Eq. 5.29). The curves show the neutral fraction evolution obtained using the integration steps $\Delta t_{\rm r}$ indicated in the legend. *Bottom panel:* relative difference between the numerically computed evolution shown in the top panel and the exact result, Eq. 5.35. Thanks to the sub-cycling, the numerical integration accurately reproduces the exact evolution of the neutral fraction for all sizes of the radiative transfer time step. Note that the simulations with time step $\Delta t_{\rm r} \leq 10^{-2}$ yr have been stopped before $t_{\rm end} = 5$ Myr because they are computationally very expensive.

neighbours) in proportion to its neutral fraction. Unless noted otherwise, the results presented in the following have been obtained with this new version of TRAPHIC. They may therefore differ slightly from those presented in Pawlik & Schaye (2008). We discuss these differences in detail in App. 5.C, to which the reader is referred.

5.4.1 Test 0: Sub-cycling the photo-ionisation rate equation

We start by testing the sub-cycling approach to the computation of the non-equilibrium neutral fraction of gas exposed to ionising radiation that we have introduced in Sec. 5.3.2. Our aim is to demonstrate that, given a flux impinging on a gas parcel (or, equivalently, a photo-ionisation rate experienced by this parcel), the sub-cycling allows for an accurate computation of the evolution of its ionisation state, independent of the size of the radiative transfer time step $\Delta t_{\rm r}$.

In close analogy to Test 0 in Iliev et al. (2006b) we simulate the evolution of the ionisation

state of an optically thin gas parcel with hydrogen number density $n_{\rm H} = 1$ cm^{-3}. The simulation starts with a fully neutral parcel at time t = 0. We then apply a flux of $F = 10^{12}$ s^{-1} cm^{-2} hydrogen-ionising photons with a black-body spectrum $B_\nu(\nu, T_{\rm bb})$ of characteristic temperature $T_{\rm bb} = 10^5$ K. Consequently, the parcel becomes highly ionised. After $t = 0.5$ Myr we switch off the ionising flux and the parcel only recombines. The simulation ends at $t_{\rm end} = 5$ Myr. Throughout the simulation we assume a constant gas temperature $T = 10^4$ K (note that this is in contrast to the test described in Iliev et al. 2006b, where the temperature evolution was followed self-consistently). This simplification will allow us to analytically derive the evolution of the neutral fraction with which our numerical results will then be compared. We will consider the combined evolution of the neutral fraction and the temperature of an optically thin gas parcel exposed to ionising radiation in Chapter 7.

We simulate the evolution of the gas parcel's neutral fraction $\eta = 1 - \chi$ by numerically integrating the photo-ionisation rate equation (see Eq. 5.4),

$$\frac{d}{dt}\eta = \alpha(T) n_{\rm e} \chi - \Gamma \eta, \tag{5.29}$$

employing the sub-cycling procedure described in Sec. 5.3.2. Recall that the sub-cycling integrates Eq. 5.29 explicitly using sub-cycle steps $\delta t \equiv f\tau_{\rm eq} \leq \Delta t_{\rm r}$. The dimensionless parameter f controls the accuracy of the integration. The recombination coefficient $\alpha(T)$ is given by Eq. 5.28 and the photo-ionisation rate Γ is (see Eq. 5.24)

$$\Gamma = \bar{\sigma} \int_{\nu_0}^{\infty} d\nu \, \frac{4\pi J_\nu(\nu)}{h_{\rm p}\nu}. \tag{5.30}$$

Using $\bar{\sigma} = 1.49 \times 10^{-18}$ cm^{-2} appropriate for the black body-spectrum $B_\nu(\nu, T_{\rm bb})$ under consideration (cp. Eq. 5.27) and $4\pi J_\nu(\nu)/(h_{\rm p}\nu) = F B_\nu(\nu, T_{\rm bb}) / \int_{\nu_0} d\nu \, B_\nu(\nu, T_{\rm bb})$, the photo-ionisation rate becomes $\Gamma = 1.49 \times 10^{-6}$ s^{-1}.

Eq. 5.29 can also be integrated analytically[9]. To see this, we write it in the form

$$\frac{d\chi}{dt} = -b(\chi - \chi_+)(\chi - \chi_-), \tag{5.31}$$

where

$$\chi_\pm \equiv \frac{a}{2b}\left(-1 \pm \sqrt{1 + \frac{4b}{a}}\right), \tag{5.32}$$

$$a \equiv \Gamma^{-1}, \tag{5.33}$$

$$b \equiv n_{\rm H}\alpha. \tag{5.34}$$

Eq. 5.31 is a differential equation of Riccati type. Its integration by separation of variables yields

$$\chi(t) = \frac{\chi_+ - \chi_- \exp[(-bt + C)(\chi_+ - \chi_-)]}{1 - \exp[(-bt + C)(\chi_+ - \chi_-)]}. \tag{5.35}$$

The integration constant C is fixed by the initial condition $\chi(t_0) = \chi_0$,

$$C = (\chi_+ - \chi_-)^{-1} \ln \frac{\chi_0 - \chi_+}{\chi_0 - \chi_-} + bt_0. \tag{5.36}$$

[9]This is a standard result from kinetic theory. For a discussion in the astrophysical literature see, e.g., Dove & Shull (1994).

In Fig. 5.1 we show the result of the simulation and compare it to the analytical result, which we will refer to as the exact result. The top panel shows the evolution of the neutral fraction for simulations using time steps $\Delta t_{\rm r} = 5 \times$ (10^{-6},10^{-4}, 10^{-2}, 10^{0}, 10^{2}, 10^{4} yr), which span 10 orders in magnitude. Note that the photo-ionisation rate implies a photo-ionisation time of only $\tau_{\rm ion} \equiv \Gamma^{-1} \approx 0.02$ yr and that the recombination time is $(\alpha n_{\rm H})^{-1} \approx 0.1$ Myr. The bottom panel shows the relative difference between the numerically computed evolutions shown in the top panel and the exact result. The agreement is excellent, with the numerical evolution never deviating by more than 10% from the exact result. This small deviation can be further reduced by lowering the value of the parameter f that controls the size of the sub-cycle steps[10]. The calculation presented here employed $f = 0.01$.

In conclusion, we have shown that with our sub-cycling approach we are able to accurately follow the evolution of the ionisation state of a gas parcel, regardless of the size of the radiative transfer time step $\Delta t_{\rm r}$ (assuming that the impinging flux is correctly computed over this time step), which was our main motivation to introduce the sub-cycling. It allows us to perform the radiative transfer and correctly compute the neutral fractions using radiative transfer time steps whose sizes are independent (and generally much larger) of the occurring photo-ionisation and recombination times, which are often impractically small.

Having established our method to solve the photo-ionisation rate equation, which comprises an important building block of our numerical implementation of TRAPHIC, we can now confidently turn to testing TRAPHIC's performance in radiative transfer problems. This will be the subject of Secs. 5.4.2 to 5.4.5.

5.4.2 Test 1: HII region expansion in a uniform medium

In this section we consider the problem of a steady ionising source emitting $\dot{\mathcal{N}}_\gamma$ mono-chromatic photons of frequency $h_{\rm p}\nu = 13.6$ eV per unit time, which is turned on in a static, initially neutral, uniform medium of constant hydrogen number density $n_{\rm H}$. This is a standard test problem, for which there exists a well-known analytical solution (for a text book discussion see Dopita & Sutherland 2003).

In equilibrium, the number of photons emitted by the source has to compensate the number of recombinations within the surrounding, stationary, ionised region, the so-called Strömgren sphere. Assuming that the Strömgren sphere is fully ionised, i.e. $\chi \equiv 1$, its radius $r_{\rm s}$ is therefore given by the balance equation

$$\dot{\mathcal{N}}_\gamma = \frac{4}{3}\pi r_{\rm s}^3 \alpha_{\rm B}(T) n_{\rm H}^2. \tag{5.37}$$

The evolution of the spherical, fully ionised region towards the equilibrium Strömgren sphere is described by the following equation for its radius $r_{\rm I}$, the ionisation front,

$$4\pi r_{\rm I}^2 n_{\rm H} \frac{dr_{\rm I}}{dt} = \dot{\mathcal{N}}_\gamma - 4\pi \int_0^{r_{\rm I}} dr\, r^2 \alpha_{\rm B}(T) n_{\rm H}^2(r), \tag{5.38}$$

which, for the case of constant density $n_{\rm H}(r) = n_{\rm H}$ that is of interest here, reads

$$4\pi r_{\rm I}^2 n_{\rm H} \frac{dr_{\rm I}}{dt} = \dot{\mathcal{N}}_\gamma - \frac{4}{3}\pi r_{\rm I}^3 \alpha_{\rm B}(T) n_{\rm H}^2. \tag{5.39}$$

[10] In the simulations with time step $\Delta t_{\rm r} < f \times \Gamma^{-1}$ (here: in the simulations using $\Delta t_{\rm r} = 5 \times 10^{-6}$ yr) the integration accuracy is controlled by the size of $\Delta t_{\rm r}$. This is the reason why the relative error for the simulation with time step $\Delta t_{\rm r} = 5 \times 10^{-6}$ yr is smaller than that for the simulation with time step $\Delta t_{\rm r} = 5 \times 10^{-4}$ yr.

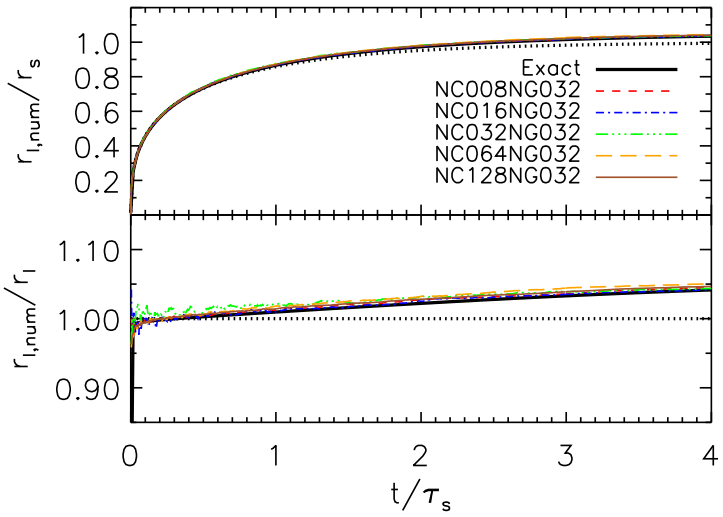

Figure 5.2: Test 1. The evolution of the ionisation front for the angular resolutions $N_{\rm c} = 8, 16, 32, 64$ and 128, as indicated in the legend. The spatial resolution is fixed ($N_{\rm SPH} = 64^3$, $\tilde{N}_{\rm ngb} = 32$). The top panel shows the position of the ionisation front $r_{\rm I,num}$ normalised by the Strömgren radius $r_{\rm s}$ as a function of time. The thick black solid curve shows a numerical reference solution obtained with a one-dimensional, grid-based radiative transfer code (see text). The black dotted curve shows the analytic reference solution, Eq. 5.41, which has been obtained by assuming $\chi \equiv 1$ throughout the ionised region. The results from the numerical simulations employing TRAPHIC closely match the numerical reference solution. The bottom panel shows the position of the ionisation fronts of the top panel divided by the analytic reference solution. Note that the analytic reference solution slightly differs from the numerical reference solution, due to the simplifying assumptions inherent to the analytic approach (see also the discussion of Eq. 5.43).

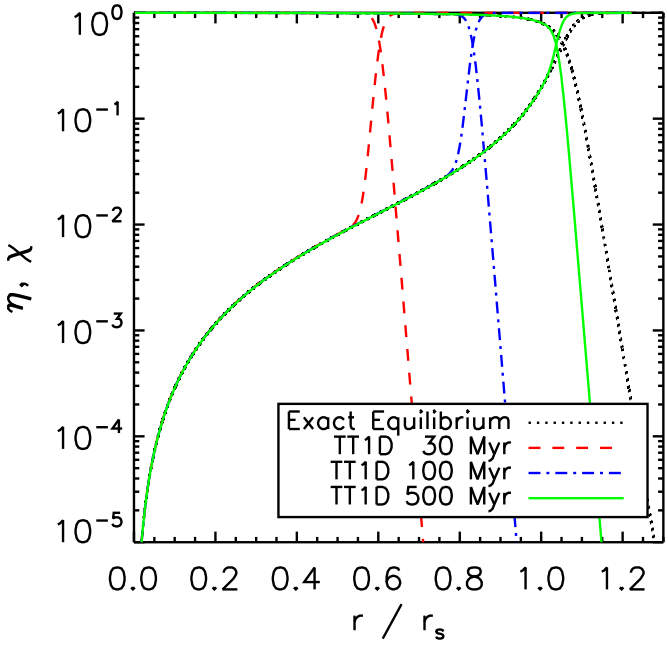

Figure 5.3: Test 1. Neutral and ionised fractions obtained from Eq. 5.43 (dotted black curves), which is the exact equilibrium solution, and from simulations with our reference code TT1D at times $t = 30$ Myr (red dashed curves), 100 Myr (blue dot-dashed curves) and 500 Myr (green solid curves). The simulations with TT1D yield results that are identical to the exact equilibrium solution at all radii for which photo-ionisation equilibrium has been reached, i.e. for radii well inside the ionised region. This excellent agreement justifies the use of TT1D for obtaining accurate reference solutions. Note that, for the chosen parameters, the equilibrium position of the ionisation front is at $r = 1.05 r_{\rm s}$ and thus at a slightly larger radius than implied by the commonly employed analytical approximation Eq. 5.41.

Introducing the new variables $\xi \equiv r_{\rm I}/r_{\rm s}$ and $\tau \equiv t/\tau_{\rm s}$, where the Strömgren time scale $\tau_{\rm s} = 1/(\alpha_{\rm B} n_{\rm H})$ is the recombination time in a fully ionised gas, we arrive at the differential equation

$$\frac{d\xi}{d\tau} = \frac{1-\xi^3}{3\xi^2}, \tag{5.40}$$

the solution of which reads

$$r_{\rm I}(t) = r_{\rm s}(1-e^{-t/\tau_{\rm s}})^{1/3}. \tag{5.41}$$

Hence, the ionisation front reaches the Strömgren sphere after a few Strömgren times $\tau_{\rm s}$ and stays static thereafter.

In reality the neutral fraction inside the ionised region is, however, not zero, but varies smoothly with the distance to the ionising source. We therefore invoke the commonly employed definition of the ionisation front as the radius at which the neutral fraction equals 50 per cent, i.e. $\eta = 0.5$. The equilibrium neutral fraction $\eta_{\rm eq}(r) = \lim_{t\to\infty}\eta(r)$ can be obtained from (e.g. Osterbrock 1989)

$$\frac{\eta_{\rm eq}(r) n_{\rm H}}{4\pi r^2} \int d\nu\, \dot{\mathcal{N}}_\gamma(\nu) e^{-\tau_\nu} \sigma_\nu = \chi_{\rm eq}^2(r) n_{\rm H}^2 \alpha_{\rm B}, \tag{5.42}$$

which can be rewritten to give the quadratic equation

$$\eta_{\rm eq}^2(r) - \left(\int d\nu\, \frac{\dot{\mathcal{N}}_\gamma(\nu) e^{-\tau_\nu}}{4\pi r^2 n_{\rm H} \alpha_{\rm B}} \sigma_\nu + 2 \right) \eta_{\rm eq}(r) + 1 = 0, \tag{5.43}$$

where the optical depth $\tau_\nu(r)$ is given by

$$\tau_\nu(r) = n_{\rm H} \sigma_\nu \int_0^r dr'\, \eta_{\rm eq}(r'). \tag{5.44}$$

We refer to the neutral fraction $\eta_{\rm eq}(r)$ obtained by direct numerical integration of Eq. 5.43 as the exact equilibrium neutral fraction profile and to $\chi_{\rm eq}(r) = 1 - \eta_{\rm eq}(r)$ as the exact equilibrium ionised fraction profile.

In the following we present a suite of radiative transfer simulations demonstrating that TRAPHIC is able to accurately follow the evolution of the ionisation front around a single ionising point source. For the setup of the numerical simulations we closely follow the description of Test 1 presented in Iliev et al. (2006b). The only differences are that we employ a different spatial resolution and that we start from ionised fractions [11] $\chi = 0$ instead of $\chi = 1.2 \times 10^{-3}$. This close matching of the setup allows us to directly compare our results to the results presented in the code comparison project. In particular, we choose a number density $n_{\rm H} = 10^{-3}$ cm^{-3} and an ionising luminosity of $\dot{\mathcal{N}}_\gamma = 5 \times 10^{48}$ photons s^{-1}. The gas is assumed to have a constant temperature $T = 10^4$ K. With these values, $r_{\rm s} = 5.4$ kpc and $\tau_{\rm s} = 122.4$ Myr.

The exact equilibrium neutral and ionised fraction profiles computed using Eq. 5.43 are shown as black dotted curves in Fig. 5.3. Note that for our choice of parameters, $r_{\rm I,eq} = 1.05\, r_{\rm s}$. The ionisation front obtained from the solution to Eq. 5.43 is thus at a slightly larger radius than the equilibrium ionisation front obtained assuming the Strömgren sphere is fully ionised (Eq. 5.41).

[11] Iliev et al. (2006b) motivated their choice of a nonzero initial ionised fraction with the presence of collisional ionisations, which we do not consider here.

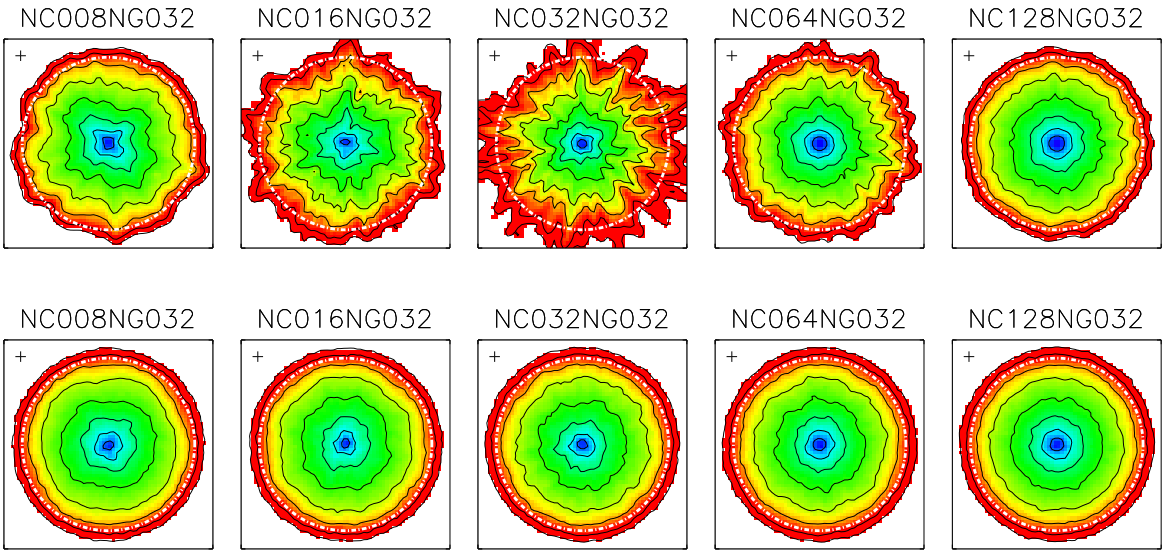

Figure 5.4: Test 1. Slice through the simulation box at $z = L_{\rm box}/2$ showing the neutral fraction at the end of the simulation ($t_{\rm r} = 500$ Myr) for simulations with (bottom row) and without (top row) resampling of the density field. The angular resolution increases from $N_{\rm c} = 8$ in the left-most to $N_{\rm c} = 128$ in the right-most column, as indicated in the panel titles. The spatial resolution is fixed to $N_{\rm SPH} = 64^3$, $\tilde{N}_{\rm ngb} = 32$ and is indicated by the cross of length $2\langle\tilde{h}\rangle$ in the upper left corner of each panel. Black contours show neutral fractions of $\eta = 0.9, 0.5, \log\eta = -1, -1.5, -2, -2.5, -3, -3.5$, going from the outside in. The white dot-dashed circle indicates the Strömgren sphere, which should be, and is, just inside to the $\eta = 0.5$ contour. The colour scale is logarithmic and has a lower cut-off of $\log\eta = -5$ (see Fig. 7.14 in Chapter 7 for a colour bar). Note that the resampling strongly suppresses the particle noise seen in the top-row panels.

The last observation indicates that the analytic solution given by Eq. 5.41 generally fails to provide an accurate reference solution that can be used to judge the validity of the numerical results obtained with a new radiative transfer scheme like TRAPHIC, due to its simplification of the problem. We therefore additionally employ the numerical solution obtained with our spherically symmetric mesh-based radiative transfer code TT1D, that we have mentioned in Sec. 5.4, in our comparisons below. In Fig. 5.3 we compare the neutral (ionised) fraction profiles obtained in simulations with TT1D to the exact equilibrium solution. The spatial resolution and the size of the time step employed in these simulations have been chosen such as to achieve numerical convergence. At radii where photo-ionisation equilibrium has been reached, the results obtained with TT1D are in excellent agreement with the exact equilibrium solution. At $t = 500$ Myr, i.e. after about 4 recombination times, equilibrium has been reached for most of (but not all of) the final ionised volume, as expected.

With accurate reference solutions at hand, we now turn to discuss the performance of TRAPHIC in the present test problem. We have set up the initial conditions described above in a simulation box of length $L_{\rm box} = 13.2$ kpc containing $N_{\rm SPH} = 64^3$ SPH particles[12]. The ionising source is located in the centre. The box boundary is photon-transmissive. We assign

[12]We note that Iliev et al. (2006b) employed $N_{\rm cell} = 128^3$ cells, with the ionising source located in one of the corners of the box.

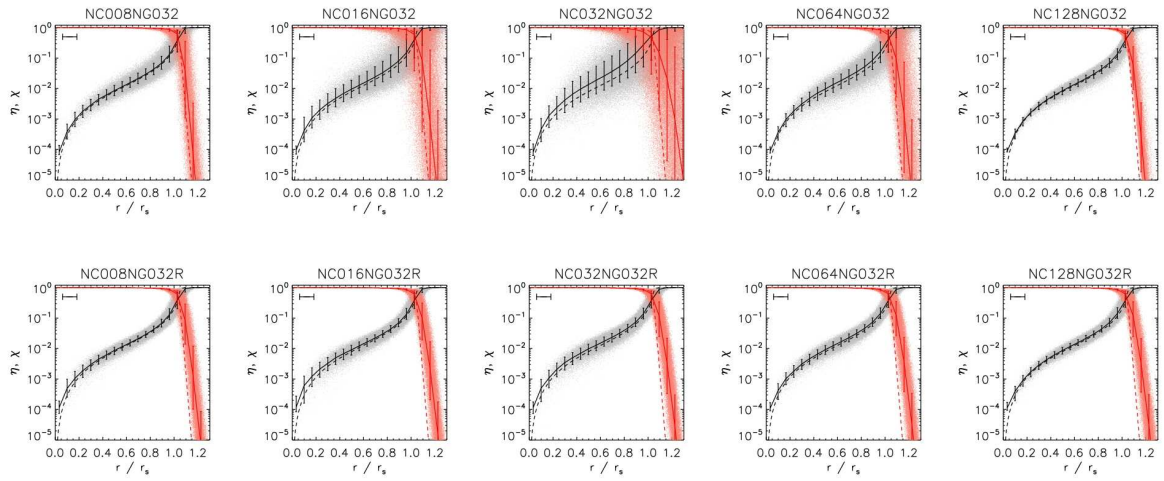

Figure 5.5: Test 1. Profiles of neutral and ionised fraction at the end of the simulation ($t_\mathrm{r} = 500$ Myr) for simulations with (bottom row) and without (top row) resampling of the density field. The spatial resolution is fixed to $N_\mathrm{SPH} = 64^3$, $\tilde{N}_\mathrm{ngb} = 32$ and is indicated by the horizontal error bars in the upper left corner of each panel. The angular resolution increases from $N_\mathrm{c} = 8$ in the left-most to $N_\mathrm{c} = 128$ in the right-most column, as indicated in the panel titles. The panels therefore directly correspond to those shown in Fig. 5.4. The grey (light red) points show the neutral (ionised) fraction of each particle. The solid black (red) curve shows the median neutral (ionised) fraction in spherical bins and the error bars show the corresponding 68.3% confidence intervals. The dashed black (red) curves show the exact solution, obtained with TT1D.

each SPH particle a mass $m = n_\mathrm{H} m_\mathrm{H} L_\mathrm{box}^3 / N_\mathrm{SPH}$. The positions of the SPH particles are chosen to be glass-like (White 1996). Glass-like initial conditions yield a more regular distribution of the particles within the box as compared to Monte Carlo sampling of the density field and are thus more suitable for the simulation of the current problem (see also our discussion in App. 5.D). The SPH smoothing kernel is computed and the SPH densities are found using the SPH formalism implemented in GADGET-2, with $N_\mathrm{ngb} = 48$.

We perform 5 simulations, increasing the angular resolution by factors of two from $N_\mathrm{c} = 8$ to $N_\mathrm{c} = 128$. The number of neighbours employed for the transport of radiation is fixed to $\tilde{N}_\mathrm{ngb} = 32$. Hence all 5 simulations employ the same spatial resolution. The time step is set to $\Delta t_\mathrm{r} = 10^{-2}$ Myr. In Fig. 5.2 we show the evolution of the ionisation front radius, which we determined by taking the average over the positions of all particles that have a neutral fraction $0.4 < \eta < 0.6$. For all 5 simulations, the position of the ionisation front never deviates more than 5 per cent from the analytic solution, Eq. 5.41, comparable to what has been found with other codes as reported in the Cosmological Radiative Transfer Code Comparison Project (Iliev et al. 2006b). Note that the deviations from the analytic solution can mainly be attributed to the fact that the analytic approach provides only an approximate expression for the radius of the ionisation front, because it erroneously assumes $\chi \equiv 1$. In fact, all simulations nearly perfectly follow the numerical reference solution and approach the proper asymptotic limit $r_\mathrm{I,eq} = 1.05\, r_\mathrm{s}$.

The top row of Fig. 5.4 shows the neutral fraction in a slice through the centre of the simulation box at $t_\mathrm{r} = 500$ Myr, which marks the end of the simulation, for each of the 5 simulations. As we already noted, the ionisation front is at the expected position. As is true for all other

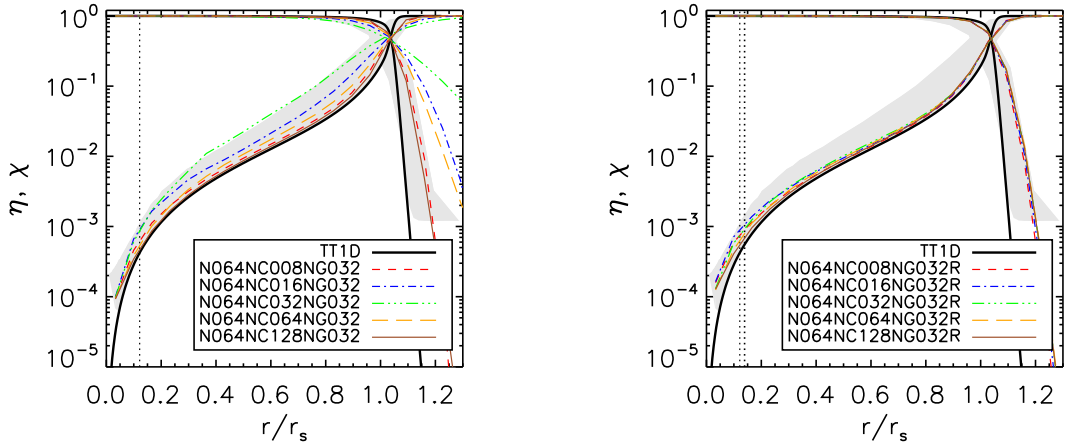

Figure 5.6: Test 1. Comparison to Iliev et al. (2006b). Spherically averaged neutral and ionised fractions within the Strömgren sphere at $t_{\rm r} = 500$ Myr for different angular resolutions, as indicated in the legend. The profiles in the left-hand (right-hand) panel correspond to simulations without (with) resampling the density field. The spatial resolution is fixed ($N_{\rm SPH} = 64^3$, $\tilde{N}_{\rm ngb} = 32$). The thick black solid curves correspond to the exact profile obtained with our reference code TT1D. The vertical dotted line marks the radius r = $2\langle\tilde{h}\rangle$, corresponding to the spatial resolution employed. In the right-hand panel, the additional (right-most) vertical dotted line indicates the radius corresponding to the spatial resolution $2\langle h\rangle$ of the SPH simulations, which is the scale on which particle positions are randomly displaced during the resampling. The grey bands show the range of neutral and ionised fractions found by other codes as reported in Iliev et al. (2006b). There, the simulations were initialised with an ionised fraction $\chi = 1.2 \times 10^{-3}$, which explains the cut-off exhibited by the grey band at large distances $r/r_{\rm s} \gtrsim 1.2$.

surfaces of constant neutral fraction shown, the ionisation front clearly exhibits the expected spherically symmetric shape, although it is noisy in some of the simulations. The amount of noise depends on the ratio of the angular and spatial resolutions employed. For $N_{\rm c} = 8$ (left-most panel in the top row), the average number of neighbours per emission or transmission cone is high, $\tilde{N}_{\rm ngb}/N_{\rm c} = 4$ and, as a result, numerical noise arising from the representation of the continuous density field with discrete SPH particles is suppressed. With increasing angular resolution the average number of neighbours per cone decreases and the contours become more noisy. The noise level reaches a maximum for $N_{\rm c} = \tilde{N}_{\rm ngb}$ (middle panel in the top row). For higher angular resolutions, the probability of finding no neighbours inside an emission or transmission cone becomes high and a large number of ViPs are created. The ratio of the number of ViPs to the number of SPH particles enclosed by the ionisation front for the simulation with angular resolution $N_{\rm c} = 8, 16, 32, 64$ and 128 is $\approx 0, 0.003, 0.06, 0.5$ and 0.9, resp. The ViPs placed in empty cones regularise the neutral fraction of the ionised density field by distributing the photons they absorb amongst their $\tilde{N}_{\rm ngb}$ SPH neighbours using (photon-conserving) SPH interpolation.

The panels in the top row of Fig. 5.5 show profiles of the neutral and ionised fraction around the ionising source at $t = 500$ Myr. Each grey (light red) dot represents the neutral (ionised) fraction of an individual particle, and the solid black (red) curves with error bars show the median neutral (ionised) fraction in spherical bins. They are compared to the dashed black (red) curves that indicate the exact results obtained with TT1D. The agreement between the results obtained with TRAPHIC and the exact result is generally very good. We note that this good

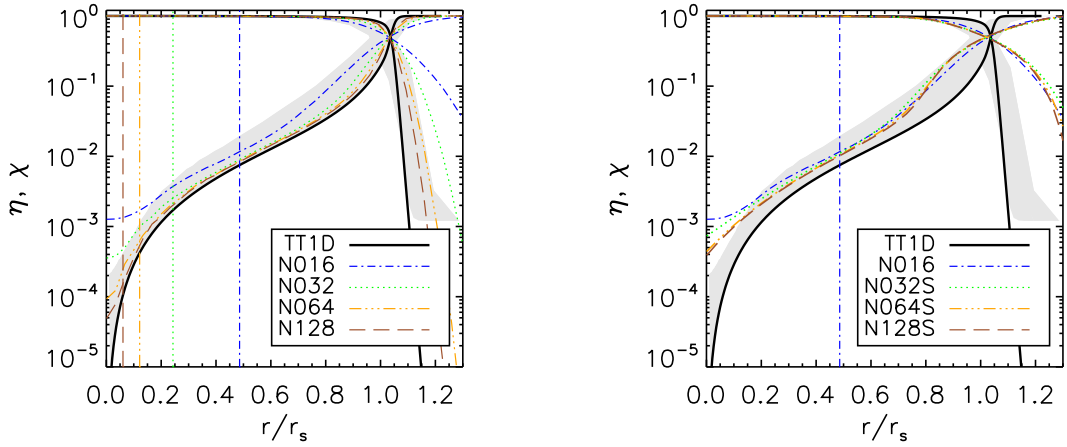

Figure 5.7: Test 1. Spherically averaged neutral and ionised fractions within the Strömgren sphere at $t_r = 500$ Myr. The simulations all have the same angular resolution ($N_c = 8$) and employ the same number of neighbours ($\tilde{N}_{ngb} = 32$), but use a different number of SPH particles, increasing from $N_{SPH} = 16^3$ to $N_{SPH} = 128^3$ in factors of 2^3. The black solid curves correspond to the exact profiles, obtained with our reference code TT1D. The grey bands show the range of neutral and ionised fractions found by other codes as reported in Iliev et al. (2006b). Left-hand panel: For each simulation the spatial resolution is marked by a vertical line (in colour and line-style identical to the corresponding profile) at radius $2\langle\tilde{h}\rangle$. The higher the spatial resolution, the more closely the exact profile is approached. Right-hand panel: The profile corresponding to the lowest spatial resolution simulation ($N_{SPH} = 16^3$, blue dot-dashed line) is repeated from the left-hand panel. The profiles of all other simulations have been smoothed over the spatial resolution element $2\langle\tilde{h}\rangle$ of the lowest spatial resolution simulation, corresponding to the radius marked by the vertical line. The profiles become nearly identical after smoothing them to the same resolution.

agreement also holds at earlier times, when the ionised sphere is still rapidly expanding, which we explicitly demonstrate for the high angular resolution simulation ($N_c = 128$) in App. 5.C. Small deviations from the exact result occur for the simulations with $N_c = 16, 32$ and 64 due to the noise they exhibit that we have already discussed above. The panels shown here illustrate this discussions in a more quantitative manner.

In the left-hand panel of Fig. 5.6 we plot the neutral and ionised fraction averaged in spherical shells as a function of distance to the star, for all 5 simulations, to perform a comparison with the results obtained with other radiative transfer codes as reported in the cosmological radiative transfer code comparison project (Iliev et al. 2006b). The range of neutral and ionised fraction found in the code comparison project simulations are indicated by the grey bands. Except for the $N_c = 32$ run, for which the neutral contours were most noisy (see Fig. 5.4), all our simulations agree very well with the results published in the comparison project. The deviations of the results obtained with TRAPHIC from the exact neutral fraction profile obtained with TT1D, that were also visible in the top row panels of Fig. 5.5, can be explained by the particle noise seen in Fig. 5.4. Due to the fuzzy structure exhibited by the neutral fraction contours, a range of neutral fractions can simultaneously be found within each spherical shell. The profiles obtained from the numerical simulation with TRAPHIC should therefore not be directly compared to the exact profile, i.e. the solution of Eq. 5.43, but to the profile that results after locally averaging the exact profile along the radial direction. The fact that the deviations from the exact result exhibited by the results published in the comparison project are relatively large

illustrates the computational difficulties in obtaining accurate three-dimensional solutions of the radiative transfer equation even in a simple test problem like the one presented here.

To investigate the effect of particle noise on the neutral fraction profile we apply the resampling technique introduced in Sec. 4.4.5, Chapter 4. We perform a series of 5 simulations that are identical to the simulations presented above, except that every 10th radiative transfer time step the particle positions are randomly perturbed within their SPH spheres of influence. The densities are not recalculated after the positions have been changed due to the resampling, because this would generate fluctuations in the neutral hydrogen density which would increase the recombination rate due to an increased gas clumping factor and lead to a smaller Strömgren sphere. The resulting neutral fraction profiles are shown in the right-hand panel of Fig. 5.6. All profiles are now in close agreement with each other and with the exact result. The panels in the bottom row of Fig. 5.4 show the neutral fraction in a slice through the centre of the simulation box from the simulations with resampling. Clearly, resampling strongly suppresses the particle noise visible in the panels in the top row of Fig. 5.4, yielding nearly spherical neutral fraction contours. This effect of resampling is further confirmed by the panels in the bottom row of Fig. 5.5, which show the median neutral and ionised fractions in spherical bins as well as the neutral and ionised fraction of each particle in the simulations that employed the resampling recipe.

We now investigate the dependence of the equilibrium neutral and ionised fraction profile on the spatial resolution by varying $N_{\rm SPH}$, the number of particles employed in the simulation. Because TRAPHIC is explicitly photon-conserving, we expect that the radiative transfer in a homogeneous medium is essentially independent of the spatial resolution (see e.g. the discussion in Mellema et al. 2006), except for a trivial smoothing. For each of the simulations with angular resolution $N_{\rm c} = 8, 32$ and 128 and $\tilde{N}_{\rm ngb} = 32$ presented above, we performed three additional simulations, at lower ($N_{\rm SPH} = 16^3, 32^3$) and higher ($N_{\rm SPH} = 128^3$) spatial resolutions, but otherwise identical to the fiducial ($N_{\rm SPH} = 64^3$) case. We will focus on the $N_{\rm c} = 8$ runs[13], but note that the $N_{\rm c} = 32$ and $N_{\rm c} = 128$ series show a similar behaviour.

The equilibrium neutral and ionised fraction profiles are shown in the left-hand panel of Fig. 5.7. For all spatial resolutions the ionisation front is at nearly the same radius. It can furthermore be seen that when the spatial resolution is increased, the equilibrium neutral fraction follows the exact result more closely. The simulation employing the fiducial spatial resolution ($N_{\rm SPH} = 64^3$) is almost converged. The differences in the neutral fraction profiles between the simulations using different numbers of particles are fully consistent with the corresponding spatial resolutions, as is demonstrated in the right-hand panel of Fig. 5.7. There, we smooth the neutral fraction profiles obtained in the simulations employing $N_{\rm SPH} = 32^3, 64^3$ and 128^3 particles over the spatial resolution element of the lowest resolution simulation ($N_{\rm SPH} = 16^3$), the size of which is indicated by the vertical line. The smoothed profiles match the neutral fraction profile obtained in the low spatial resolution simulation almost exactly. This shows that decreasing the spatial resolution does not introduce any artefacts. The solution obtained by TRAPHIC is the converged solution smoothed over the adopted spatial resolution.

Finally, we show how the size of the time step $\Delta t_{\rm r}$ affects the outcome of our simulations. We again concentrate on the simulation[14] with angular resolution $N_{\rm c} = 8$ (and $N_{\rm SPH} = 64^3$, $\tilde{N}_{\rm ngb} = 32$), noting that the simulations of higher angular resolution exhibit a similar behaviour. In Fig. 5.8 we show the evolution of the ionisation front for four different choices for the size

[13]These runs have been performed with the version of TRAPHIC described in Pawlik & Schaye (2008). We have not repeated them with the current code version, since this version only differs in the manner virtual particles are treated. For the low angular resolution employed here, however, no virtual particles are created.

[14]See footnote 13

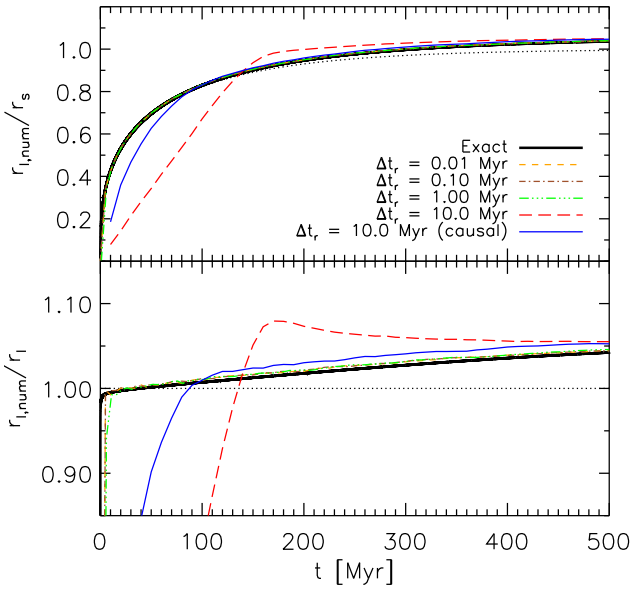

Figure 5.8: Test 1. Effect of the size of the time step. We show the evolution of the ionisation fronts for four simulations with $N_{\rm c} = 8$, $N_{\rm SPH} = 64^3$, $\tilde{N}_{\rm ngb} = 32$ and time steps $\Delta t_{\rm r} = 0.01, 0.1, 1$ and 10 Myr, resp, as indicated in the legend. After an initial phase, the evolution of the ionisation fronts becomes independent of the size of the radiative transfer time step. The duration of this initial phase can be shortened by applying the causal correction explained in the text, as we explicitly demonstrate for the simulation with time step $\Delta t_{\rm r} = 10$ Myr.

of the radiative transfer time step, $\Delta t_{\rm r} = 0.01, 0.1, 1$ and 10 Myr. In order to keep the angular sampling the same, at each radiative transfer step we split the emission of photons over 10, 100 and 1000 random orientations of the emission cone tessellation of the ionising source for the simulations employing $\Delta t_{\rm r} = 0.1, 1$ and 10 Myr, resp. Differently from what is done for all other simulations described in this section, photon packets that are emitted by the source in a certain orientation are transmitted further downstream and can propagate over multiple inter-particle distances during a single time step. We follow each photon packet until it has either been absorbed or left the simulation box, to properly solve the time-independent radiative transfer equation for the large time steps under consideration.

From Fig. 5.8 we see that the evolution of the ionisation front for the simulations with time step $\Delta t_{\rm r} = 0.1, 1$ and 10 Myr is delayed with respect to the evolution of the ionisation front for the simulation with time step $\Delta t_{\rm r} = 0.01$ Myr. This delay increases with the size of the time step, being barely visible for the simulation using $\Delta t_{\rm r} = 0.1$ Myr. The delay arises because the neutral fraction is only updated at the end of each radiative transfer time step. Photons that have been absorbed during the transport over a single time step but that have not been used to advance the neutral fraction during the subsequent sub-cycling of the rate equation are therefore only re-inserted in the transport process at the beginning of the next time step and are thus delayed. From Fig. 5.8 it can, however, be seen that after a few time steps, the ionisation front catches up to agree with the ionisation front obtained in the simulation using $\Delta t_{\rm r} = 0.01$ Myr. We note that we have also tried to re-insert these photons immediately after they have been absorbed, by integrating the rate equation already at the end of each transport cycle (without updating the neutral fraction) to obtain the number of photons that have been erroneously counted as being absorbed (because of the assumption of a constant neutral fraction). We refer to this manner of transporting photons as causal, because of its similarity with the causal transport employed in Mellema et al. (2006). The causal correction, i.e. the re-insertion of these photons in the transport process within the same radiative transfer time step over which they have been absorbed, indeed reduces the observed delay of the ionisation front (see the blue

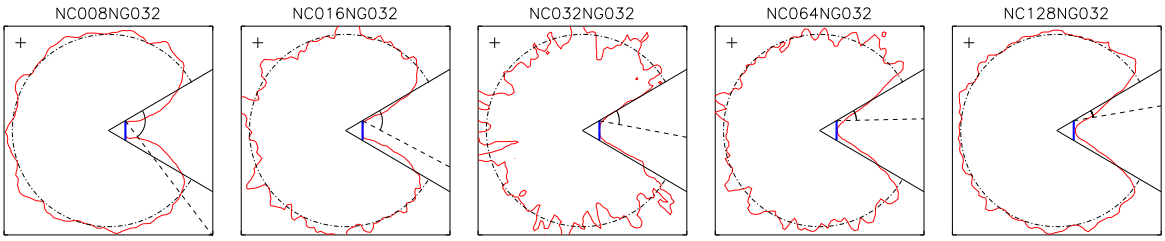

Figure 5.9: Test 2. Slice through the simulation box at $z = L_{\rm box}/2$ showing the ionisation front (red solid line) at time $t_{\rm r} = 80$ Myr around an ionising source sitting in the centre of the simulation box. The black dot-dashed circle shows the expected ionisation front position. The thick blue vertical line indicates an obstacle opaque to ionising photons and the black solid lines trace out the boundaries of the shadow this obstacle is expected to throw. The cross and the black dashed line indicate the spatial and angular resolution, respectively, as described in the text. The spatial resolution is fixed to $N_{\rm SPH} = 64^3, \tilde{N}_{\rm ngb} = 32$. The angular resolution increases from $N_{\rm c} = 8$ in the left-most panel to $N_{\rm c} = 128$ in the right-most panel, in factors of 2.

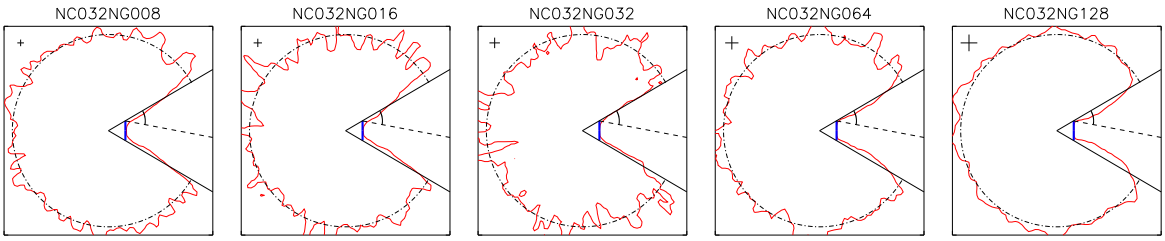

Figure 5.10: Test 2. Same as Fig. 5.9, but with the angular resolution fixed to $N_{\rm c} = 32$ and the spatial resolution decreasing, from $N_{\rm SPH} = 64^3, \tilde{N}_{\rm ngb} = 8$ in the left-most panel to $N_{\rm SPH} = 64^3, \tilde{N}_{\rm ngb} = 128$ in the right-most panel, increasing the number of neighbours $\tilde{N}_{\rm ngb}$ in factors of 2.

thin solid line in Fig. 5.8).

In summary, in this section we showed that TRAPHIC is able to reproduce the expected equilibrium neutral fraction around an ionising source embedded in a homogeneous medium, as well as the dynamical evolution towards it. Because the radiative transfer is explicitly photon-conserving, the spatial resolution only determines the scale over which the converged solution is smoothed. We have furthermore seen that the performance of TRAPHIC is stable with respect to variations in the size of the time step. Particle noise due to the discrete nature of SPH simulations is small except for the choice of parameters $N_{\rm c} \approx \tilde{N}_{\rm ngb}$. The noise can be successfully suppressed by applying a resampling technique that periodically perturbs the positions of the SPH particles within their spatial resolution element.

5.4.3 Test 2: Ionisation front shadowing by an opaque obstacle

In the absence of scattering interactions, photons propagate along straight lines into the direction set at the time of their emission. Consequently, opaque obstacles throw sharply defined

shadows. In this section we are mainly interested in studying the properties of the shadow thrown by an opaque obstacle exposed to ionising radiation from a single point source, as obtained with TRAPHIC. At the same time, we will extend the study of particle noise presented in Sec. 5.4.2 to include other choices for the parameter $\tilde{N}_{\rm ngb}$. All of the simulations presented in this section have been performed with the original version of TRAPHIC presented in Pawlik & Schaye 2008. We have verified for a few individual simulations that our current, improved version, in which the distribution of photons absorbed by virtual particles amongst the neighbouring SPH particles is done using a more self-consistent weighting scheme than the one that was used in the original publication (see our discussion in Sec. 5.4), produces nearly identical results.

The geometry of our test problem closely follows the description of the shadow test in Mellema et al. (2006). We consider a source emitting $\dot{\mathcal{N}}_\gamma = 10^{54}$ photons s^{-1}, each of hydrogen-ionising energy $h_{\rm p}\nu = 13.6$ eV, residing in an initially neutral, static hydrogen-only field of constant number density $n_{\rm H} = 1.87 \times 10^{-4}$ cm^{-3} and temperature $T = 10^4$ K. The Strömgren radius (Eq. 5.37) corresponding to this set of parameters is $r_{\rm s} = 0.965$ Mpc and the Strömgren time is $\tau_{\rm s} = 654.3$ Myr. For the numerical simulation a star particle is placed in the centre of a box of size $L_{\rm box} = 1$ Mpc. The boundaries of the box are photon-transmissive. The density field is sampled using $N_{\rm SPH} = 64^3$ gas particles with mass $m = n_{\rm H} m_{\rm H} L_{\rm box}^3 / N_{\rm SPH}$ at glass-like positions. The particle densities are found using the SPH interpolation implemented in GADGET-2, with $N_{\rm ngb} = 48$. We furthermore place an infinitely thin opaque disc perpendicular to the x-axis at a distance of 0.08 Mpc along the x-axis from the star (thick blue vertical lines in Figs. 5.9-5.13). The y and z coordinates of the disc centre are identical to those coordinates of the star. Photons that cross the disc are removed.

We performed a series of radiative transfer simulations (with time step $\Delta t_{\rm r} = 10^4$ yr), using different choices for the parameters $\tilde{N}_{\rm ngb}$, which sets the spatial resolution if the total number of SPH particles is fixed, and $N_{\rm c}$, which sets the angular resolution. The results are shown in Figs. 5.9 - 5.13, displaying a slice through the simulation box at $z = L_{\rm box}/2$. In each panel, the black dash-dotted circle shows the expected position of the ionisation front (Eq. 5.41) at time $t_{\rm r} = 80$ Myr, which marks the end of the simulation. The black solid lines emerging from the star at the centre of the slice show the boundaries of the shadow expected to be thrown by the opaque disc (thick blue vertical line). In the top-left corner of each panel we indicate the spatial resolution by a cross of length $2\langle\tilde{h}\rangle$ corresponding to the average diameter of the sphere containing $\tilde{N}_{\rm ngb}$ neighbours. The angular resolution is indicated by the angle ω enclosed by the black dashed line and the upper shadow boundary, where ω is determined using Eq. 4.9. It indicates the *maximum* angle photons can theoretically diverge from the shadow boundary into the shadow region, given the chosen angular resolution $N_{\rm c}$.

The position of the ionisation front (the iso-surface for which the neutral fraction $\eta = 0.5$) at time $t_{\rm r} = 80$ Myr as obtained with TRAPHIC is shown by the red solid line. In all panels, that is for all spatial and angular resolutions, the ionisation front is found at the proper position, in agreement with our findings of Sec. 5.4.2. The shadow thrown by the opaque disc is always sharp. We now discuss the dependence of the results on the chosen spatial and angular resolutions.

In Fig. 5.9 we show the ionisation front obtained in simulations employing a fixed spatial resolution, $\tilde{N}_{\rm ngb} = 32$, but varying angular resolution, ranging from $N_{\rm c} = 8$ in the left-most to $N_{\rm c} = 128$ in the right-most panel. The most prominent difference between the results of the different simulations is the noisiness of the contour tracing out the ionisation front. The angular resolution study presented here is very similar to the one in the last section. For the lowest

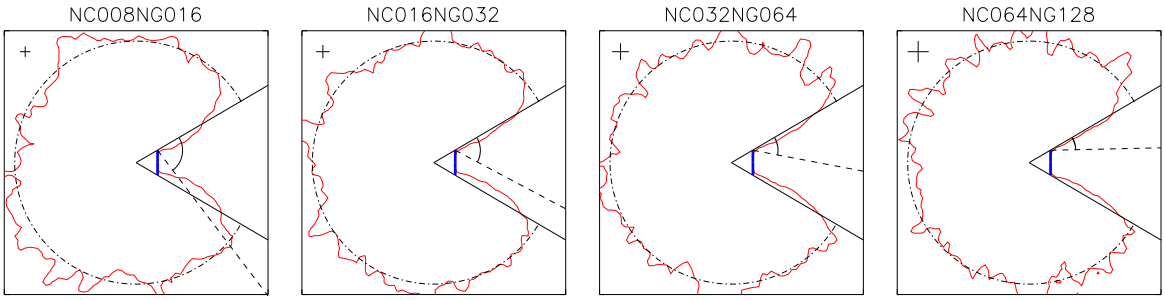

Figure 5.11: Test 2. Same as Fig. 5.9, but fixing the ratio between spatial and angular resolution to $\tilde{N}_{\rm ngb}/N_{\rm c} = 2$ ($N_{\rm SPH} = 64^3$).

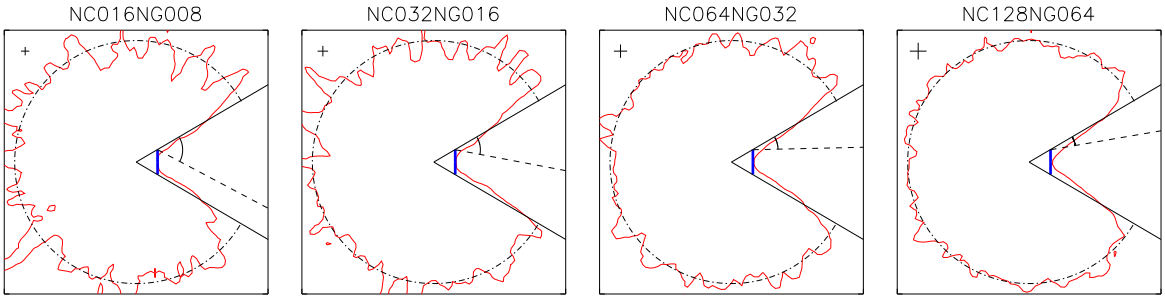

Figure 5.12: Test 2. Same as Fig. 5.9, but fixing the ratio between spatial and angular resolution to $\tilde{N}_{\rm ngb}/N_{\rm c} = 1/2$ ($N_{\rm SPH} = 64^3$).

angular resolution, $N_{\rm c} = 8$, the ionisation front is very smooth due to the large number of neighbours within each emission and transmission cone. The noise increases with the angular resolution until it reaches a maximum for $N_{\rm c} = \tilde{N}_{\rm ngb}$. For higher angular resolutions, particle noise is efficiently suppressed due to the large number of ViPs that are placed in empty cones and that distribute the photons they absorb amongst their $\tilde{N}_{\rm ngb}$ SPH neighbours using (photon-conserving) SPH interpolation.

From Fig. 5.9 it can furthermore be seen how the sharpness of the shadow thrown by the opaque disc depends on the angular resolution. For the lowest angular resolution, the shadow is somewhat blurred, though not nearly as much as the angular resolution would imply. Increasing the angular resolution yields slightly sharper shadows. However, if the angular resolution is increased beyond $N_{\rm c} = \tilde{N}_{\rm ngb}$, the shadows become slightly less sharp. This is because the photons absorbed by ViPs are distributed amongst the neighbouring gas particles using SPH interpolation and the interpolation procedure does not know about the shadow region. The slight diffusion of photons across the shadow boundary is in this case consistent with the spatial resolution.

In Fig. 5.10 we show the results of the simulations where we fixed the angular resolution to $N_{\rm c} = 32$, but varied the spatial resolution by changing $\tilde{N}_{\rm ngb}$. The trends visible in Fig. 5.9

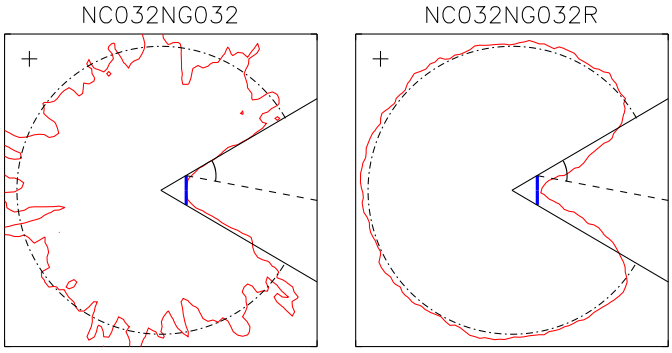

Figure 5.13: Test 2. *Left-hand panel:* Identical to the middle panels of Figs. 5.9 and 5.10. *Right-hand panel:* Same as left-hand panel, except for the fact that in the simulation we periodically re-sampled the density field, resulting in a strong suppression of the particle noise seen in the left-hand panel. Note the (small amount of) diffusion of photons across the shadow boundary due to the motion of the transmission cone apexes.

can also be observed here. The ionisation front is most noisy and the shadow is sharpest for $N_{\rm c} = \tilde{N}_{\rm ngb}$. For $\tilde{N}_{\rm ngb} > N_{\rm c}$, noise due to the discreteness of the particles employed for the transport of photons is suppressed by the large number of neighbours per cone, but the shadow is slightly blurred. The shadow becomes sharper for a smaller number of neighbours, since generally not all of the solid angle will be covered by the neighbours, an effect that becomes more important for smaller numbers of neighbours. For $\tilde{N}_{\rm ngb} < N_{\rm c}$ the ionisation front becomes smoother due to the regularising effect of the SPH interpolation from ViPs, which also leads to a small diffusion of photons across the shadow boundary, consistent with the spatial resolution.

In Figs. 5.11 and 5.12 we keep the ratio $\tilde{N}_{\rm ngb}/N_{\rm c}$ fixed at $\tilde{N}_{\rm ngb}/N_{\rm c} = 2$ and $\tilde{N}_{\rm ngb}/N_{\rm c} = 1/2$, resp. In the first case there are on average 2 neighbours per cone, whereas in the second case there is on average one neighbour in every second cone. From Fig. 5.11 it is clear that the shadow does get sharper when the angular resolution is increased, although the effect is small, since the shadow is always very sharp. Because we keep the ratio $\tilde{N}_{\rm ngb}/N_{\rm c}$ fixed at 2, the number of ViPs employed in the simulation stays low for all angular resolutions and the shadows are not visibly diffused by the SPH interpolation of absorbed photons from the ViPs. Furthermore, the noisiness of the ionisation front remains constant throughout the parameter range. This is because the noise is primarily set by the ratio $\tilde{N}_{\rm ngb}/N_{\rm c}$ if $\tilde{N}_{\rm ngb} > N_{\rm c}$. In Fig. 5.12, on the other hand, there is a substantial probability for creating a ViP per cone. Since the absolute number of ViPs present in the simulation increases with increasing angular resolution $N_{\rm c}$, the noise decreases with $N_{\rm c}$.

In the last section (see bottom row of Fig. 5.4) we employed a resampling technique to decrease the noise exhibited by the neutral fraction contours. Recall from Section 4.4.2 that the apexes of the transmission cones are attached to the positions of the SPH particles. Hence, resampling results in slight shifts in the position of each transmission cone apex, on the scale of the spatial resolution employed in the SPH simulation. This shifting is expected to lead to a small diffusion of photons across the expected shadow boundary. Such a diffusion due to particle resp. apex motion will also occur in radiation-hydrodynamical simulations because of the movement of the SPH particles. It is therefore interesting to study the properties of the shadow thrown by an opaque obstacle in the case of resampling.

In Fig. 5.13 we show the results of a simulation which employs the same parameters as used for the simulation presented in the middle panels of Fig. 5.9 and 5.10, but with an additional resampling of the hydrogen density field every 10th radiative transfer time step. As in the last section, the resampling is performed without changing the hydrogen density, since this would

lead to an enhanced recombination rate. Numerical noise is successfully suppressed by the random perturbations given to the positions of the SPH particles. Consequently, the ionisation front appears significantly smoother. The degree of photon diffusion into the shadow region is small and does not significantly degrade the angular resolution of the radiative transfer. This is because the diffusion scale is set by the spatial resolution employed in the SPH simulation. Therefore, well-defined shadows will be thrown as long as the obstacle is spatially resolved. The effect of resampling on the properties of shadows will be further discussed in Sec. 5.4.5.

In summary, in this section we showed that TRAPHIC is able to produce a well-defined shadow behind an opaque obstacle, with the shadow sharpness in full agreement with the chosen spatial and angular resolutions. In fact, the shadows are much sharper than implied by the formal angular resolution, thanks to the angular adaptivity inherent to TRAPHIC. For a fixed angular resolution, the shadows are sharpest for $N_{\rm c} = \tilde{N}_{\rm ngb}$. They are slightly broadened by photon diffusion for both $N_{\rm c} < \tilde{N}_{\rm ngb}$ and $N_{\rm c} > \tilde{N}_{\rm ngb}$, due to the increased coverage of the solid angles traced out by the transmission cones with SPH particles for an increasing number of neighbours $\tilde{N}_{\rm ngb}$ and the SPH interpolation of the photons absorbed by ViPs, resp. We confirmed our finding of the last section that unless $\tilde{N}_{\rm ngb} = N_{\rm c}$, noise due to the discreteness of the particles on which the transport of photons takes place is small, since it is suppressed by either the large number of neighbours per cone (if $N_{\rm c} < \tilde{N}_{\rm ngb}$) or the large number of ViPs employed (if $N_{\rm c} > \tilde{N}_{\rm ngb}$). The resampling technique that we have already used in Sec. 5.4.2 is confirmed to be very effective at suppressing particle noise. We have seen that resampling the density field does not severely degrade the angular resolution, even though it leads to a small shift of the cone apexes. As long as the opaque obstacle is spatially resolved by the SPH simulation, a well-defined shadow will still be thrown.

The ability to produce sharp shadows is one of the main requirements a radiative transfer code has to pass. The results of this section, together with the results of Test 1, which showed that TRAPHIC is able to reproduce the expected neutral fraction within a spherically symmetric HII region, indicate that TRAPHIC can be used to perform the transport of ionising photons in arbitrarily complex geometries. This will be the subject of Test 4 presented below. Before that, however, we will discuss the performance of TRAPHIC in the important problem of the spherically symmetric expansion of an HII-region in a centrally peaked density field.

5.4.4 Test 3: HII region expansion in a centrally peaked density field

The spherically averaged gas density profile in the dense central regions of star-forming galaxies can often be described by a simple power-law relation between gas density and distance from the galaxy centre. For example, the central parts of galaxies embedded in a Navarro, Frenk, & White (1997) dark matter halo will obey a spherically averaged gas density profile that is inversely proportional to the distance from the halo centre (assuming that the gas distribution follows that of the dark matter). Dark matter simulations (e.g., Springel et al. 2008) and first-principle considerations (He 2009) suggest that the Navarro, Frenk, & White (1997) profile provides a universal description of the distribution of matter in galaxy halos. It is thus important to verify that our radiative transfer scheme is able to accurately compute the propagation of ionisation fronts in such a centrally peaked density field. In this section we therefore study the propagation of an ionisation front in the singular density profile

$$n_{\rm H}(r) = n_0 \frac{r_0}{r}, \tag{5.45}$$

where n_0 is the density at radius $r = r_0$.

An analytic solution to the ionisation front evolution in such a density profile was derived by Mellema et al. (2006), as follows. Assuming a fully ionised sphere, the position of the ionisation front driven by a source with constant ionising luminosity $\dot{\mathcal{N}}_\gamma$ is given by Eq. (5.38). Making use of the density profile Eq. 5.45, this equation reads

$$\frac{dr_\mathrm{I}}{dt} = \frac{\dot{\mathcal{N}}_\gamma}{4\pi n_0 r_0} r_\mathrm{I}^{-1} - n_0 r_0 \alpha_\mathrm{B}(T). \tag{5.46}$$

Substituting $u \equiv r_\mathrm{I}^{-1}$, the last equation transforms into

$$\frac{du}{dt} = u^2 \left(-\frac{\dot{\mathcal{N}}_\gamma}{4\pi n_0 r_0} u + n_0 r_0 \alpha_\mathrm{B}(T) \right). \tag{5.47}$$

Introducing the notation

$$\tilde{u} \equiv \frac{\dot{\mathcal{N}}_\gamma}{4\pi n_0^2 r_0^2 \alpha_\mathrm{B}} u \tag{5.48}$$

$$\tilde{t} \equiv \frac{4\pi n_0^3 r_0^3 \alpha_\mathrm{B}^2}{\dot{\mathcal{N}}_\gamma} t, \tag{5.49}$$

the ionisation front evolution is described by

$$\frac{d\tilde{u}}{d\tilde{t}} = \tilde{u}^2 (1 - \tilde{u}). \tag{5.50}$$

The solution to Eq. (5.50) can be expressed in terms of Lambert's W function (e.g., Corless et al. 1996),

$$\tilde{u}(\tilde{t}) = \frac{1}{1 + W\left(z e^{z - \tilde{t}}\right)} \tag{5.51}$$

$$z = \frac{1}{\tilde{u}(0)} - 1. \tag{5.52}$$

Imposing the initial condition $r_\mathrm{I}(0) = 0$ and transforming back to the original variables,

$$r_\mathrm{I}(t) \;=\; r_\mathrm{s} \left\{ 1 + W\left[-\exp\left(-\frac{r_0}{r_\mathrm{s}\tau_\mathrm{s}} t - 1 \right) \right] \right\} \tag{5.53}$$

$$\tag{5.54}$$

Hereby, $r_\mathrm{s} = \dot{\mathcal{N}}_\gamma / (4\pi n_0^2 r_0^2 \alpha_\mathrm{B})$ is the (generalised) Strömgren radius and $\tau_\mathrm{s} = (n_0 \alpha_\mathrm{B})^{-1}$ is the (generalised) Strömgren time, i.e. the characteristic time on which equilibrium is approached.

We will employ Eq. 5.54 as a reference solution and refer to it as an analytic approximation. In Sec. 5.4.2 we have, however, seen that the assumption of a fully ionised sphere may not yield a sufficiently accurate expression for the evolution of the ionisation front. As in Sec. 5.4.2, we will therefore additionally compare the results of our simulations obtained with TRAPHIC to the solution derived numerically using our spherically symmetric radiative transfer code TT1D, to which we refer as the exact solution.

We set up the density profile Eq. 5.45 around an ionising source located at the centre of a simulation box with side length 7.5 kpc. We use the parameters $n_0 = 0.015$ cm^{-3}, $r_0 = 5$ kpc which are identical to those used in the corresponding test problem by Mellema et al.

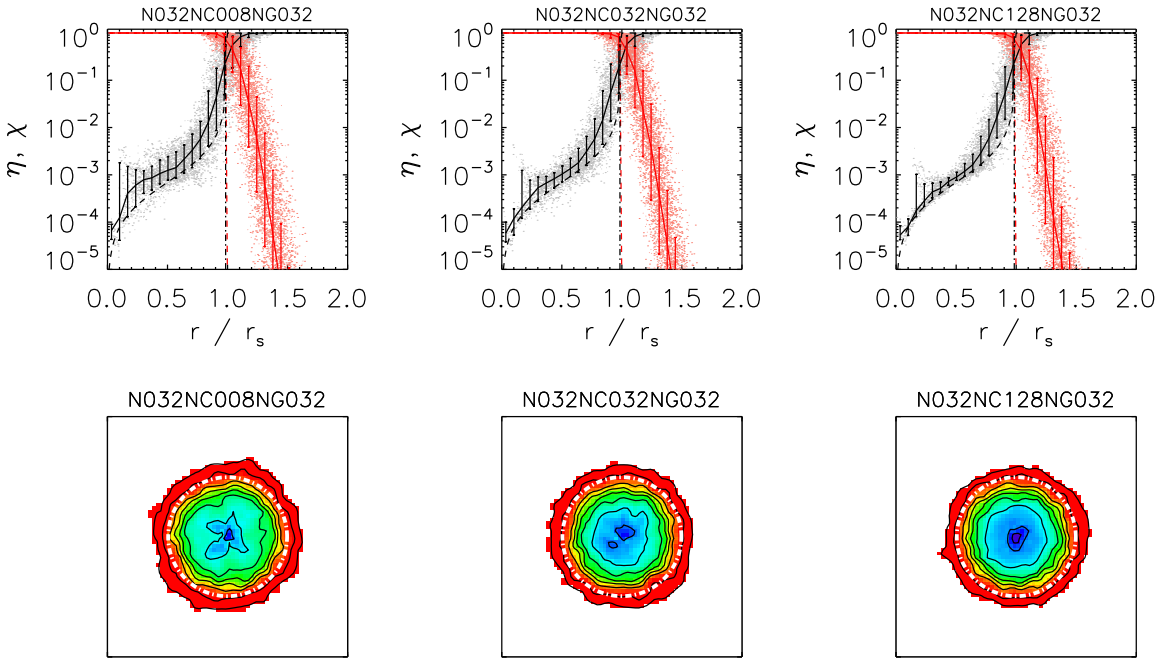

Figure 5.14: Test 3. *Top row:* Profiles of the neutral and ionised fraction at $t = 10$ Myr. The angular resolution increases from $N_\mathrm{c} = 8$ in the left-most panel and $N_\mathrm{c} = 32$ in the middle panel to $N_\mathrm{c} = 128$ in the right-most panel. The grey (light red) points show the neutral (ionised) fraction of each particle. The solid black (red) curve shows the median neutral (ionised) fraction in spherical bins, the error bars the corresponding 68.3% confidence intervals. The dashed black (red) curves show the exact solution and the vertical dot-dashed black line indicates the ionisation front position from Eq. 5.54. The dashed red curve and the black dot-dashed curve are nearly on top of each other. *Bottom row:* neutral fraction in a slice through the simulation box at $z = L_\mathrm{box}/2$, corresponding to the panels shown in the top row. Black contours show neutral fractions of $\eta = 0.9, 0.5, \log\eta = -1, -1.5, -2, -2.5, -3, -3.5, -4$, going from the outside in. The white dot-dashed circle indicates the ionisation front position from Eq. 5.54. The colour scale is logarithmic and has a lower cut-off of $\log\eta = -5$ (see Fig. 7.14 in Chapter 7 for a colour bar). See text for discussion.

(2006). The central source has a luminosity of $L_\gamma = 10^{51}$ s^{-1} hydrogen-ionising photons. Our parameter choices imply a Strömgren radius $r_\mathrm{s} \sim 1.86$ kpc and a Strömgren time $\tau_\mathrm{s} \sim 8.16$ Myr.

The density profile is obtained by applying a coordinate transformation to particles that are initially uniformly distributed (at glass-like positions), which is described in App. 5.D. In short, particles are moved radially away from their original (glass-like) positions to stretch the local mean particle distance such that the SPH volume the particles occupy becomes proportional to their distance from the source. After the particles have been placed, their densities are calculated using the SPH formalism of GADGET-2, with $N_\mathrm{ngb} = 48$. All simulations presented in this section are initialised with 32^3 particles at glass-like positions, which results in ≈ 10000 (≈ 2000) SPH particles within the central sphere of radius 3 kpc (2 kpc). We employ this relatively small number of particles (and hence a correspondingly low spatial resolution) in order to more closely resemble simulated halos in cosmological simulations. We note that (for the angular resolution $N_\mathrm{c} = 8$) we have performed simulations of both lower and higher spatial

resolution to convince ourself that these simulations show the expected behaviour.

The boundaries of the simulation box are assumed to be transmissive, i.e. photons leaving the box are lost from the computational domain. We use $\tilde{N}_{\rm ngb} = 32$ radiative transfer neighbours. In Secs. 5.4.2 and 5.4.3 we have seen that the resampling procedure introduced in Chapter 4 strongly reduces artefacts caused by the particular realization of particle positions. In all the simulations presented here we therefore resample the density field every 10th time step. The radiative transfer time step is set to $\Delta t_{\rm r} = 10^{-3}$ Myr. We furthermore split, during each radiative transfer time step, the emission of photons by the source over 32 random orientations of its emission cone tessellation. We found that this increase in angular sampling is required in order to to obtain sufficiently accurate results (see also the discussion on the related effect of angular resolution below). We have made no attempt to optimise this number.

In Fig. 5.14 we show profiles of the neutral fraction η and ionised fraction χ and images of the neutral fraction η in a slice through the box centre at $t = 10$ Myr for three simulations that have increasing angular resolutions: $N_{\rm c} = 8$ (left-most panel), $N_{\rm c} = 32$ (middle panel) and $N_{\rm c} = 128$ (right-most panel). For all three simulations the median neutral (ionised) fraction, as indicated by the solid black (red) curve with error bars (which are the 68.3% confidence intervals) in the top panels of Fig. 5.14, closely agrees with the exact solution. Inside the ionised region, away from the ionisation front, the agreement is best for the simulation with the highest angular resolution. This is because a higher angular resolution implies a larger number of cones into which the source simultaneously emits photon packets, which implies an increased angular sampling.

At low angular resolutions, fewer SPH particles receive radiation during a time step. These particles then only recombine. As a result, their neutral fraction temporarily drifts away from its expected value, introducing scatter. Such a behaviour is commonly encountered in Monte Carlo radiative transfer schemes (for discussions see, e.g., Maselli, Ciardi, & Kanekar 2009; Altay, Croft, & Pelupessy 2008). It illustrates the Monte Carlo aspect of TRAPHIC. For the angular resolution $N_{\rm c} = 128$, the median neutral fraction inside the ionisation front is nearly indistinguishable from the exact solution[15]. The remaining difference with respect to the exact solution as well as the small deviation of the median from the exact solution close to the ionisation front is due to the employed low spatial resolution, which implies an effective smoothing of the exact solution (which corresponds to infinitely high spatial resolution), as we already discussed in Sec. 5.4.2.

In conclusion, we have shown that TRAPHIC is able to accurately reproduce the expected growth of ionised regions in centrally peaked density fields. This is important since such density fields are typical for the first sites of star formation in the cosmological simulations we wish to employ TRAPHIC. The results also illustrated the Monte-Carlo aspect of TRAPHIC: although the spherically symmetric problem is formally independent of angular resolution, we found that the agreement with the exact solution increases with angular resolution. This is because of the increased number of cones into which photon packets are simultaneously emitted, which increases the angular sampling of the computational domain. The same result can, however, be obtained by distributing the photons to be emitted during a given time step over an increased number of random orientations of the emission cone tessellation (or, alternatively, by decreasing the time step).

[15]Note, however, that there are still a few particles (around $r \approx 0.2 r_{\rm s}$) that due to a lack of angular sampling are not sufficiently frequently updated with ionising radiation and therefore have a neutral fraction that is too high.

5.4.5 Test 4: Expansion of multiple HII regions in a cosmological density field

Until now we have considered highly idealised test problems. We studied the performance of TRAPHIC in simulations of the growth of spherically symmetric ionised regions in a uniform medium and a centrally peaked density profile, and we analysed its capability to produce shadows behind opaque obstacles. In this section we will consider a more complex test that combines all the difficulties posed by the problems discussed so far: we test the propagation of ionisation fronts around multiple sources in a static cosmological density field. The test is designed to resemble important aspects of state-of-the-art simulations of the epoch of reionisation. Its parameters are taken from Test 4 of the Cosmological Radiative Transfer Code Comparison Project (Iliev et al. 2006b). The simulations presented there were limited to solving the time-independent radiative transfer equation. To allow an accurate comparison, we will therefore focus on solving the time-independent radiative transfer equation, but we will briefly discuss the differences to a corresponding time-dependent simulation.

The initial conditions are provided by a snapshot (at redshift $z \approx 8.85$) from a cosmological N-body and gas-dynamical simulation performed using the cosmological (uniform-mesh) PM+TVD code of Ryu et al. (1993). The simulation box is $L_{\rm box} = 0.5\ h^{-1}$ comoving Mpc on a side, uniformly divided into $N_{\rm cell} = 128^3$ cells. The initial temperature is fixed at $T = 100$ K everywhere. The halos in the simulation box were found using a friends-of-friends halo finder with a linking length of 0.25. The ionising sources are chosen to correspond to the 16 most massive halos in the box. We assume that these have a black-body spectrum $B_\nu(\nu, T)$ with temperature $T = 10^5$ K. The ionising photon production rate is assumed to be constant and assigned assuming that each source lives for $t_{\rm s} = 3$ Myr and emits $f_\gamma = 250$ photons per atom during its lifetime. Hence, the number of ionising photons emitted per unit time is

$$\dot{\mathcal{N}}_\gamma = f_\gamma \frac{M \Omega_{\rm b}}{\Omega_0 m_{\rm H} t_{\rm s}}, \tag{5.55}$$

where M is the total halo mass, $\Omega_0 = 0.27$, $\Omega_b = 0.043$ and $h = 0.7$. For simplicity, all sources are assumed to switch on at the same time. The boundary conditions are photon-transmissive. Outputs are produced at $t = 0.05, 0.1, 0.2, 0.3$ and 0.4 Myr.

With respect to the original test setup described above, we require three changes. First, since our code does not yet solve for the temperature of the gas, we assume a constant temperature of $T = 10^4$ K for the ionised gas. Second, since our code currently treats only a single frequency (bin), we treat the multi-frequency problem in the grey approximation, assuming the grey photo-ionisation cross-section Eq. 5.27. The third change concerns the input density field. Since our code works directly on the set of particles used in SPH simulations, we have to Monte Carlo sample the original input density field in order to place particles in the box. We replace every grid cell i by $N^i_{\rm SPH} = M_i/m$ SPH particles (randomly distributed within the volume of the grid cell), where $M_i = \rho_i L^3_{\rm box}/N_{\rm cell}$ is the mass of the cell and m is the mass of an SPH particle. If $N^i_{\rm SPH}$ is not an integer, we draw a random number from a uniform distribution on the interval (0,1) and place an additional particle if this number is smaller than the difference between $N^i_{\rm SPH}$ and the nearest lower integer. We use $N_{\rm SPH} = N_{\rm cell} = 128^3$. Since the Monte Carlo sampling only results in the approximate equality $\sum_i N^i_{\rm SPH} \approx N_{\rm SPH}$, we adjust the particle masses a posteriori to conserve mass, i.e. $m \rightarrow m \times N_{\rm SPH}/\sum_i N^i_{\rm SPH}$. After the particles have been placed, we calculate their densities using the SPH formalism of GADGET-2, with $N_{\rm ngb} = 48$.

Note that Monte Carlo sampling the density field with $N_{\rm SPH} \simeq N_{\rm cell}$ particles yields a smaller effective resolution than that of the grid input field in low density regions (many grid

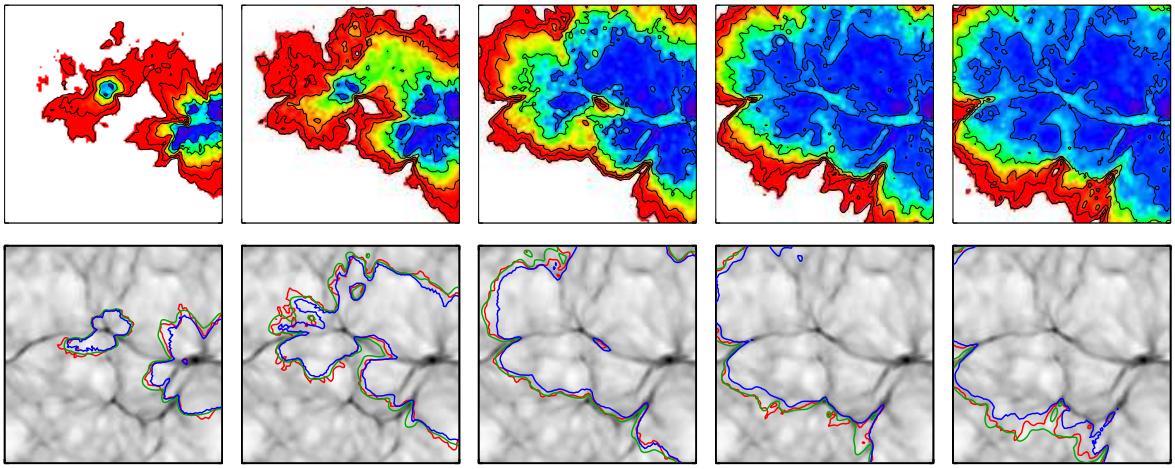

Figure 5.15: Test 4: *Top row:* neutral fraction in a slice through $z = L_{\rm box}/2$ at times $t = 0.05, 0.1, 0.2, 0.3, 0.4$ Myr (from left to right). Contours show neutral fractions $\eta = 0.9, 0.5$, $\log \eta = -1, -3$ and -5, from the outside in. The colour scale is logarithmic and has a lower cut-off of $\eta = 10^{-7}$. It is identical to the colour scale used and shown in Fig. 7.19 of the corresponding test 7 in Chapter 7. *Bottom row:* Density field in the slices shown in the top panels. Contours show ionisation fronts (neutral fraction of $\eta = 0.5$). Red contours show the results of our fiducial ($N_{\rm c} = 32, \tilde{N}_{\rm ngb} = 32$) simulation. For comparison, we show the results of C^2-RAY (green) and CRASH (blue), as reported in Iliev et al. (2006b). The agreement is excellent. *See Fig. 3 in the appendix at the end of this thesis for a coloured version.*

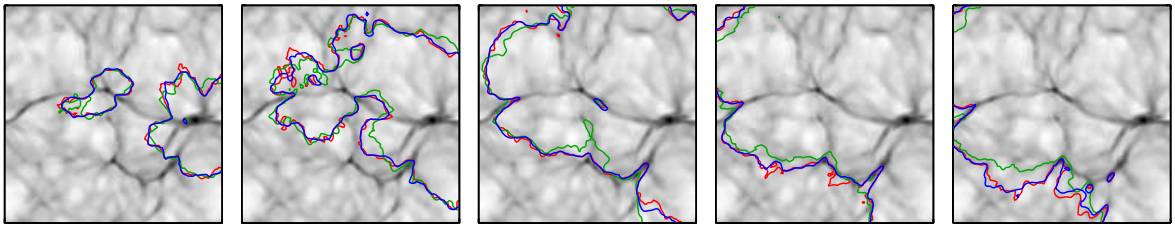

Figure 5.16: Test 4: Effect of angular resolution. The same slice as shown in Fig. 5.15, bottom row. Contours show ionisation fronts (neutral fraction $\eta = 0.5$) at times $t = 0.05, 0.1, 0.2, 0.3$ and 0.4 Myr (from left to right). Green, red and blue lines correspond to the low ($N_{\rm c} = 8$), fiducial ($N_{\rm c} = 32$) and high ($N_{\rm c} = 128$) angular resolution simulations, respectively. The fiducial simulation is already converged, even though its angular resolution $N_{\rm c} = 32$ corresponds to a relatively large cone opening angle of $\omega \approx 41$ degrees.

cells will be left empty of particles), and to a spurious higher resolution in high density regions (cells are sampled with many particles, even though there is no substructure on the scale of a single cell in the input field). Note also that because the initial conditions were specified on a uniform grid, we do not benefit from the intrinsic spatial adaptivity of TRAPHIC, effectively wasting computational resources.

We performed a set of three radiative transfer simulations with angular resolutions $N_{\rm c} = 8, 32$ and 128, which we refer to as the low angular resolution, fiducial and high angular resolution simulations, resp. Every simulation used $\tilde{N}_{\rm ngb} = 32$ neighbours. The time step was set to $\Delta t_{\rm r} = 10^{-4}$ Myr.

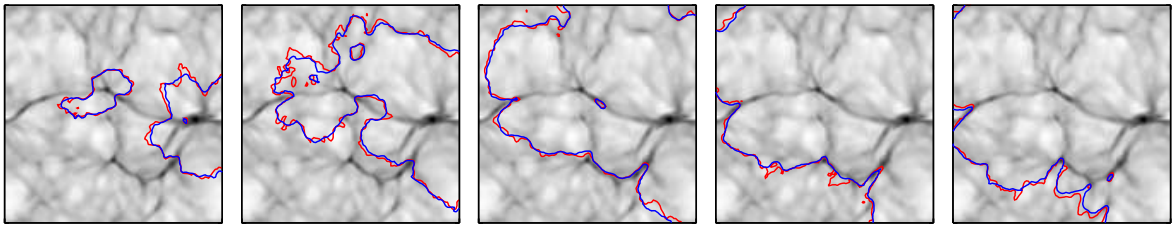

Figure 5.17: Test 4: Effect of resampling. The same slice as shown in Fig. 5.15, bottom row. Contours show ionisation fronts (neutral fraction $\eta = 0.5$) at times $t = 0.05, 0.1, 0.2, 0.3$ and 0.4 Myr (from left to right). The red contours correspond to the fiducial angular resolution simulation. The blue contours correspond to a simulation identical to the simulation employing the fiducial angular resolution, except for the fact that in this simulation we periodically (every 10th radiative transfer time step) re-sampled the density field to suppress the particle noise. Note that resampling does not visibly decrease the effective angular resolution.

In Fig. 5.15 we show the result of our fiducial simulation at times $t = 0.05, 0.1, 0.2, 0.3$ and 0.4 Myr (from left to right). The panels in the top row show images of the neutral fraction in a slice through the centre of the simulation box. Contours of neutral fraction $\eta = 0.9, 0.5$, $\log_{10} \eta = -1, -3$ and -5 have be superimposed. The panels in the bottom row repeat the $\eta = 0.5$ contour, i.e. the ionisation front, showing it on top of the input density field. It can be clearly seen that the ionisation front is delayed by the dense filaments, leading to the characteristic "butterfly" shapes of the ionised regions.

For comparison, we also show the results obtained with two other codes, the ray-tracing scheme C^2-RAY (Mellema et al. 2006; green contours) and the Monte Carlo code CRASH (Maselli, Ferrara, & Ciardi 2003; Ciardi et al. 2001; blue contours), as published in the cosmological radiative transfer code comparison project (Iliev et al. 2006b)[16]. Both C^2-RAY and CRASH are mesh codes, working directly on the uniform mesh input density field provided by the PM+TVD code of Ryu et al. (1993).

The agreement between the results of TRAPHIC and C^2-RAY resp. CRASH is very good. We have explicitly verified that this good agreement is also true for contours of lower neutral fraction (see Pawlik & Schaye 2008 and the result of Test 7 in Chapter 7). The contours from TRAPHIC are slightly noisier than those from C^2-RAY, which is expected since in addition to the particle noise affecting the radiative transfer, the Monte-Carlo sampling noise imprinted on the density field affects our simulations, particularly in the under-sampled low density regions, as already noted earlier. The noise level is, however, substantially lower than one would anticipate based on the tests presented in Secs. 5.4.2 and 5.4.3. The most likely explanation for this welcome surprise is that the presence of multiple ionising sources leads to a regularisation in the distribution of the neutral fraction (a fact that has been noted also by other authors, e.g. Trac & Cen 2007). Numerical noise arising from the representation of the continuous density field by a discrete set of particles is therefore reduced.

Differences between our results and those of C^2-RAY resp. CRASH also arise through the different treatment of the photon spectrum. Since the photo-ionisation cross-section depends

[16]The performance of two more codes was reported in Iliev et al. (2006b): FTTE (Razoumov & Cardall 2005) and SIMPLEX (Ritzerveld & Icke 2006). For clarity and since they are very similar to the results obtained with C^2-RAY and CRASH, we do not show the results obtained with FTTE (but see Test 7 in Chapter 7). We do not include the results of SIMPLEX in our comparison, since they differ considerably from those obtained with all other codes.

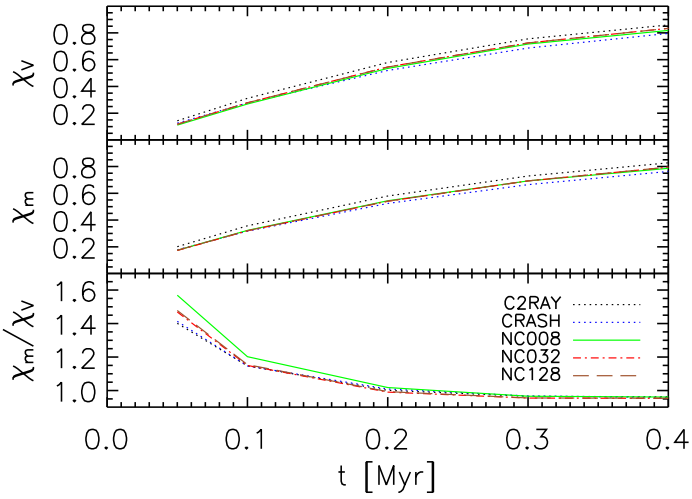

Figure 5.18: Test 4: The volume- and mass-weighted mean ionised fractions, $\chi_{\rm V}$ and $\chi_{\rm m}$, resp., averaged over the whole simulation box as a function of time, for the low, fiducial and high angular resolution simulation, as indicated in the legend. All results fall nearly on top of each other. Differences in $\chi_{\rm m}/\chi_{\rm V}$ are only noticeable when $\chi_{\rm V}$ is small. For comparison, we also show the results obtained with C^2-RAY and CRASH as reported in Iliev et al. (2006b).

on frequency (Eq. 5.2), the thickness of finite ionisation fronts (e.g. defined as $0.9 < \eta < 0.1$) and hence the position of the particular contour $\eta = 0.5$ will in part be determined by the details of the numerical implementation of the multi-frequency transport. Finally, while both C^2-RAY and CRASH follow the thermal evolution of the gas, our simulations assume a fixed gas temperature, which provides another source for the observed differences.

In Fig. 5.16 we show the ionisation fronts at times $t = 0.05, 0.1, 0.2, 0.3$ and 0.4 Myr (from left to right) for the low (green contours) and the high (blue contours) angular resolution simulations. For comparison, the contours obtained in the fiducial simulation are also shown (red). We note that the high angular resolution simulation yields neutral fraction contours that are almost identical to those obtained in our fiducial simulation, indicating numerical convergence. The low angular resolution simulation, although still in good agreement with the high angular resolution simulation, fails to properly reproduce the expected neutral fraction contours when scrutinised in detail. In the low angular resolution simulation we noticed that neutral fraction contours are sometimes slightly advanced instead of delayed by the dense filaments. The effect is small, but it becomes apparent when the contours are compared to the corresponding contours of the high angular resolution simulation (although it is barely visible in the images presented here).

Our observation agrees with the discussion of anisotropies in particle-to-neighbour transport schemes presented in Chapter 4 (see in particular its App. 4.A). There we demonstrated that when photons are transported from a given particle to its neighbours, the net transport direction is generally strongly correlated with the direction towards the centre of mass of the neighbouring particles. As a result, the transport is partly governed by the spatial distribution of the SPH particles. For cosmological simulations this implies that photons are preferentially transported along dense filaments. TRAPHIC propagates photons in cones to overcome this problem. The cones confine the photons to the solid angles they were emitted into, ensuring a correct transport of radiation on the scale of the chosen angular resolution. If the angular resolution is chosen too low to properly resolve the structures in the SPH density field, the transport is no longer independent of the geometry of the SPH simulation and artefacts may occur. In the present case, even with an angular resolution as low as $N_{\rm c} = 8$, the artefacts are small. Nevertheless, it is clear that in order to properly solve the radiative transfer equation, the angular resolution must be chosen high enough to establish numerical convergence.

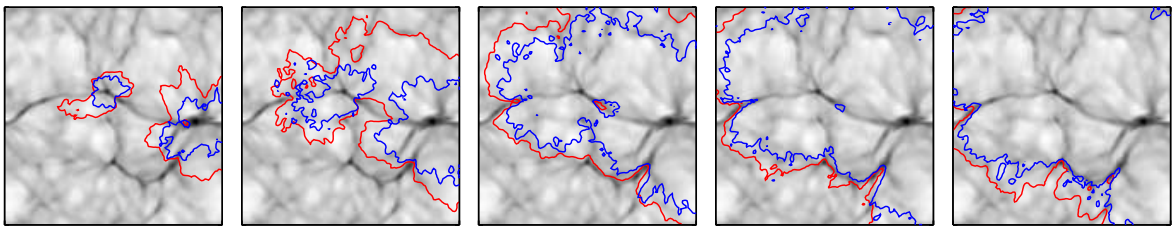

Figure 5.19: Test 4: Slice through the density field at $z = L_{\rm box}/2$. Contours show a neutral fraction of $\eta = 0.5$ at times $t = 0.05, 0.1, 0.2, 0.3$ and 0.4 Myr (from left to right). Red contours show the results of our fiducial ($N_{\rm c} = 32, \tilde{N}_{\rm ngb} = 32$) simulation (and are thus identical to the red contours shown in Fig. 5.15). Blue contours show the result of a simulation employing the same resolution ($N_{\rm c} = 32, \tilde{N}_{\rm ngb} = 32$), but using the clock of the photon packets to solve the time-dependent radiative transfer equation. Note that in the simulation solving the time-independent radiative transfer equation the ionised regions are too large, since in this simulation the ionisation fronts are initially propagating at speeds larger than the speed of light. The fact that the ionisation fronts are more noisy in the simulation that employed the clocks than in the one which did not is due to the fact that the former simulation was performed with the original (slightly noisier, see App. 5.C) version of TRAPHIC, while the latter (as all other simulations presented in this section) made use of our current version.

Fig. 5.16 shows that an angular resolution of $N_{\rm c} = 32$, which corresponds to a relatively large opening angle of $\omega \approx 41$ degrees (Eq. 4.9 in Chapter 4), is already converged. The reason why a relatively poor formal angular resolution suffices, is, as already noted in the discussion of the sharpness of shadows thrown by opaque obstacles in Sec. 5.4.3, that the photon transport with TRAPHIC is intrinsically adaptive in angle.

In Fig. 5.17 we present results for a simulation that used the resampling technique presented in Sec. 5.3.4, but which was otherwise identical to the fiducial simulation presented above. The neutral hydrogen densities of the SPH particles were not re-calculated according to the perturbed positions resulting from the resampling, but kept constant to avoid additional scatter in the density. The resampling leads to a reduction in the particle noise. The improvement is not dramatic since the noise is already very low, as noted above. Observe that the resampling does not noticeable degrade the angular resolution - shadows remain sharp.

In Fig. 5.18 we show the evolution of the mean (over all particles i) ionised fraction, both volume-weighted, i.e. $\chi_{\rm V} = \sum_i h_i^3 \chi_i / \sum_i h_i^3$, where h_i is the radius of the SPH kernel of particle i, and mass-weighted, i.e. $\chi_{\rm m} = \sum_i m_i \chi_i / \sum_i m_i$. Again, the results obtained with TRAPHIC are in excellent agreement with the results obtained with C^2-RAY and CRASH. For the latter two we obtained the mean ionised fraction by averaging the ionised fraction reported in the cosmological radiative transfer code comparison project (Iliev et al. 2006b) over all grid cells i, i.e. $\chi_{\rm V} = \sum_i \chi_i / \sum_i 1$ and $\chi_{\rm m} = \sum_i \rho_i \chi_i / \sum_i \rho_i$.

The ratio of mass-weighted and volume-weighted mean ionised fractions is at early times slightly larger for the low angular resolution simulation than for the high angular resolution simulation, as can be seen in the bottom panel of Fig. 5.18. This is another manifestation of the fact that particle-to-neighbour transport is generally not independent of the geometry of the SPH simulation, resulting in photons being preferentially transported into high (particle) density regions. It once more underlines the importance of the concept of emission and transmission cones (with sufficiently small solid angles) which TRAPHIC uses to accomplish the transport of radiation independently of the spatial distribution of the SPH particles.

Finally, we show that for the present radiative transfer problem, simulations solving the

time-dependent radiative transfer equation give a significantly different result than the simulations solving the time-independent radiative transfer equation discussed above. We carried out a simulation using $N_{\rm c} = 32, \tilde{N}_{\rm ngb} = 32$ and additionally employed the photon packet clocks to limit the distance over which photon packets can propagate during each time step. The size of the radiative transfer time step was set to $\Delta t_{\rm r} = 10^{-3}$ Myr. This time step is a factor 10 larger than the time step used for solving the time-independent radiative transfer equation in the simulations presented above, which required a smaller time step because of our particular treatment of the time-independent radiative transfer equation (see Sec. 5.3.3). The locations of the ionisation fronts (i.e. $\eta = 0.5$) obtained in this simulation are shown in Fig. 5.19 (blue curves), together with those obtained in the corresponding simulation solving the time-independent radiative transfer equation (red curves, which are identical to those in Fig. 5.15), at times $t = 0.05, 0.1, 0.2, 0.3$ and 0.4 Myr.

It is clear from Fig. 5.19 that the simulation solving the time-independent radiative transfer equation produces ionised spheres that are unphysically large. This is due to the well-known fact (see, e.g., the discussion in Abel, Norman, & Madau 1999) that ionisation fronts may propagate at speeds larger than the speed of light, if the time-independent radiative transfer equation is solved. The difference between the two simulations is larger at early times than at late times, which is expected, since in equilibrium, i.e. $t_{\rm r} \rightarrow \infty$, the results of both simulations must agree.

In summary, in this section we studied the propagation of ionisation fronts around multiple sources in a static cosmological density field. We demonstrated the importance of the concept of cones which underlies the photon transport in TRAPHIC. Without the confinement by transmission cones of sufficiently small solid angle, particle-to-neighbour transport is governed in part by the spatial distribution of the particles, resulting in the preferential transport of photons into high (particle) density regions. Thanks to the fact that TRAPHIC is adaptive in angle, a relatively modest formal angular resolution of $N_{\rm c} = 32$ is already sufficient to obtain a converged solution. Since the setup of our simulations followed the description of the corresponding test in the cosmological radiative transfer code comparison project (Iliev et al. 2006b), we were able to benchmark our radiative transfer scheme by comparing with the results obtained by the ray-tracing scheme C^2-RAY (Mellema et al. 2006) and the Monte Carlo code CRASH (Maselli, Ferrara, & Ciardi 2003; Ciardi et al. 2001). We found excellent agreement in the positions of neutral fraction contours as well as the mass and volume-weighted mean ionised fractions.

We have furthermore seen that for the test problem presented in this section, simulations solving the time-independent radiative transfer equation lead to ionised regions that are unphysically large during their early evolution. This illustrates the importance of correctly accounting for the finite speed of light when performing radiative transfer simulations to study the morphology of ionised regions that are strongly out of equilibrium.

5.5 CONCLUSIONS

We have presented an implementation of our radiative transfer scheme TRAPHIC, that we have described in Chapter 4, in the smoothed particle hydrodynamics code GADGET-2 to accomplish the transport of (mono-chromatic) hydrogen-ionising radiation in hydrodynamical simulations.

As part of this implementation we have introduced a numerical method that allows us to accurately compute the evolution of the ionised fraction of a gas parcel exposed to ionising radiation, independently of the size of the radiative transfer time step $\Delta t_{\rm r}$ employed. This decoupling of the radiative transfer time step from the time scales that govern the evolution of

the neutral fraction, i.e. from the photo-ionisation time scale $\tau_{\rm ion}$ and the recombination time scale $\tau_{\rm rec}$, is an important pre-requisite for performing efficient radiative transfer simulations. The alternative, a radiative transfer time step limited by the values for the photo-ionisation or recombination time scales, would generally be computationally infeasible, since these time scales may become very small. The method consists of sub-cycling the evolution of the neutral fraction over the radiative transfer time step in an explicitly photon-conserving manner. We have verified it by comparing results of numerical simulations of an optically thin gas parcel ionising up and recombining with the analytical solution to this problem.

We have then ran several radiative transfer simulations on static density fields and solved the radiative transfer equation, in both its time-independent and time-dependent form, in problems of increasing complexity. Throughout we have employed both analytical and numerical reference solutions to quantify TRAPHIC's performance in these problems. For the latter we have developed a spherically symmetric mesh-based radiative transfer code (TT1D). We also employed results reported in the literature (Mellema et al. 2006; Iliev et al. 2006b) that have been obtained by other radiative transfer codes in identical test problems for our comparison.

We first showed that TRAPHIC is able to accurately reproduce the expected growth of the ionised sphere around a single point source in a homogeneous medium. There we found that in addition to the number of cones $N_{\rm c}$ and the number of SPH neighbours $\tilde{N}_{\rm ngb}$, it is the ratio $N_{\rm c}/\tilde{N}_{\rm ngb}$ that directly influences the performance of TRAPHIC. It controls the amount of noise introduced by the representation of the underlying continuum physics with a discrete set of particles. This particle noise is small for both $N_{\rm c} < \tilde{N}_{\rm ngb}$ and $N_{\rm c} > \tilde{N}_{\rm ngb}$ due to the large number of neighbours per cone and the large number of ViPs, resp. For the choice of parameters $N_{\rm c} = \tilde{N}_{\rm ngb}$ the particle noise can be substantial. It can, however, be efficiently suppressed by employing the density field resampling strategy that we have suggested in Chapter 4.

We have furthermore verified that TRAPHIC is able to cast sharp shadows behind opaque obstacles, which is a main requirement for radiative transfer schemes to pass. We have shown that the sharpness of the shadows is controlled by and in agreement with the formal angular resolutions employed. In fact, we found that the shadows are much sharper than implied by that formal angular resolution. We have demonstrated that transmission cone apex motions implied by a moving set of SPH particles do not noticeably degrade the effective angular resolution and hence TRAPHIC's shadowing characteristics. TRAPHIC can therefore also be applied in dynamical simulations, in step with the hydrodynamical evolution of the SPH particles, and we will present such dynamical simulations in Chapter 6.

We also computed the growth of an ionised region in a centrally peaked density profile. The setup of this problem is characteristic for star-forming regions in cosmological structure formation simulations. This test problem clearly revealed the Monte-Carlo aspect of TRAPHIC. The numerical results obtained in simulations of this problem converged towards the exact solution with increasing number of cones $N_{\rm c}$ used, which can be explained by noting that the number of cones determines the number of directions that are simultaneously sampled.

Finally, we tested our scheme in a scaled-down version of a typical epoch-of-reionisation simulation: we studied the growth of ionised regions around multiple point sources in a cosmological density field at high redshift. Comparisons to the results obtained by other radiative transfer codes showed excellent agreement. These codes were limited to solving the time-independent radiative transfer problem. Thanks to the use of photon packet clocks, TRAPHIC may also be used to solve the time-dependent radiative transfer problem. We have repeated the simulation and performed such a time-dependent computation. We have confirmed the well-known fact that time-independent radiative transfer simulations, because they assume an

infinite speed of light, may predict too fast a growth of the ionised regions.

The fact that the results of all tests performed in this chapter are in excellent agreement with both analytically and numerically computed reference solutions confirms the validity of the concepts underlying our radiative transfer scheme TRAPHIC. The radiative transfer test problems performed in this chapter have been set up in a somewhat idealised manner to facilitate the evaluation of their results and the comparison with reference solutions. Their simplified design is, unfortunately, not suited to demonstrate the advantages of TRAPHIC over conventional radiative transfer schemes - that it is spatially adaptive, that it is implemented for use in parallel on distributed memory machines and that its computation time is independent of the number of radiation sources. TRAPHIC will unfold its true strength only in the large hydrodynamical simulations it has been developed for. We will perform such simulations in the next chapter, Chapter 6.

ACKNOWLEDGEMENTS

We thank Claudio Dalla Vecchia for stimulating discussions and help with the setup of simulations. We are grateful to Craig Booth and Benedetta Ciardi for a thorough reading of the draft version of Pawlik & Schaye (2008). A.H.P. thanks the University of Potsdam and the Max Planck Institut für Astrophysik for their hospitality where part of the work presented in this chapter has been done. He is indebted to Prof. Arkardi Pikovsky and Volker Springel for their cordiality during these stays. Some of the simulations presented here were run on the Cosmology Machine at the Institute for Computational Cosmology in Durham as part of the Virgo Consortium research programme and on Stella, the LOFAR BlueGene/L system in Groningen. This work was supported by Marie Curie Excellence Grant MEXT-CT-2004-014112.

REFERENCES

Abel T., Norman M. L., Madau P., 1999, ApJ, 523, 66

Alvarez M. A., Bromm V., Shapiro P. R., 2006, ApJ, 639, 621

Altay G., Croft R. A. C., Pelupessy I., 2008, MNRAS, 386, 1931

Ciardi B., Ferrara A., Marri S., Raimondo G., 2001, MNRAS, 324, 381

Corless, R. M.; Gonnet, G. H.; Hare, D. E. G.; Jeffrey, D. J.; and Knuth, D. E., Adv. Comput. Math. 5, 329-359

Dale J. E., Bonnell I. A., Whitworth A. P., 2007, MNRAS, 375, 1291

Dopita M. A., Sutherland R. S., 2003, Astrophysics of the diffuse universe, Springer

Dove J. B., Shull J. M., 1994, ApJ, 430, 222

Gnedin N. Y., Abel T., 2001, NewA, 6, 437

Goldstein H., 1980, Classical Mechanics, Addison-Wesley Publ. Co

Gritschneder M., Naab T., Heitsch F., Burkert A., 2007, IAUS, 237, 246

He P., 2009, arXiv, arXiv:0903.2208

Hockney R. W., Eastwood J. W., 1988, Computer Simulations Using Particles, Taylor & Francis

Iliev I. T., Mellema G., Pen U.-L., Merz H., Shapiro P. R., Alvarez M. A., 2006, MNRAS, 369, 1625

Iliev I. T., et al., 2006, MNRAS, 371, 1057

Johnson J. L., Greif T. H., Bromm V., 2007, ApJ, 665, 85

Kohler K., Gnedin N. Y., Hamilton A. J. S., 2007, ApJ, 657, 15

Maselli A., Ferrara A., Ciardi B., 2003, MNRAS, 345, 379

Petkova M., Springel V., submitted

Shampine L. F., Gear C. W., 1979, SIAM Review, Vol. 21, No. 1., pp. 1-17, Jstor.

Maselli A., Ciardi B., Kanekar A., 2009, MNRAS, 393, 171

Mellema G., Iliev I. T., Alvarez M. A., Shapiro P. R., 2006, NewA, 11, 374

Mihalas D., Weibel Mihalas B., 1984, Foundations of radiation hydrodynamics, Oxford University Press, New York

Miles R. E., 1965, Biometrika, Vol. 52, No. 3/4, pp. 636

Navarro J. F., Frenk C. S., White S. D. M., 1997, ApJ, 490, 493

Osterbrock D. E., 1989, Astrophysics of gaseous nebulae and active galactic nuclei, Palgrave Macmillan

Paschos P., Norman M. L., Bordner J. O., Harkness R., 2007, arXiv, 711, arXiv:0711.1904

Pawlik A. H., Schaye J., 2008, MNRAS, 389, 651

Press W. H., Teukolsky S. A., Vetterling W. T., Flannery B. P., 1992, Numerical recipes in C. The art of scientific computing, Cambridge University Press, 2nd ed.

Razoumov A. O., Cardall C. Y., 2005, MNRAS, 362, 1413

Ritzerveld J., Icke V., 2006, PhRvE, 74, 026704

Ryu D., Ostriker J. P., Kang H., Cen R., 1993, ApJ, 414, 1

Springel V., 2005, MNRAS, 364, 1105

Springel V., et al., 2008, MNRAS, 391, 1685

Stewart G. W., 1980, SIAM Journal on Numerical Analysis, Vol. 17, No. 3, 403

Trac H., Cen R., 2007, ApJ, 671, 1

Susa H., Umemura M., 2006, ApJ, 645, L93

White S. D. M., 1996, Cosmology and large scale structure, Proceedings of the "Les Houches Ecole d'Ete de Physique Theorique" (Les Houches Summer School), p. 349, Elsevier Scientific Publishing Company, Amsterdam

Whalen D., Norman M. L., 2007, arXiv, 708, arXiv:0708.2444

Wise J. H., Abel T., 2007, arXiv, 710, arXiv:0710.3160

Yoshida N., Oh S. P., Kitayama T., Hernquist L., 2007, ApJ, 663, 687

5.A CONSTRAINTS ON THE INTEGRATION STEP SIZE IN THE EULER DISCRETIZATION

In this section we show that when advancing the neutral fraction over a single time step $\Delta t_{\rm r}$ according to Eq. 5.21, that is using the Euler discretization, this time step has to satisfy $0 \leq \Delta t_{\rm r} \leq f\tau_{\rm eq}$ in order for the neutral fraction to obey its physical bounds. Hereby, $\tau_{\rm eq}$ is the time scale on which photo-ionisation equilibrium is approached (Sec. 5.2, Eq. 5.7) and $f < 1$ is a dimensionless parameter that will be defined below.

In the Euler discretization, the new neutral fraction $\eta(t+\Delta t_{\rm r})$ is related to the current neutral fraction $\eta(t)$ via

$$\eta(t+\Delta t_{\rm r}) = \eta(t) + \beta n_{\rm e}(1-\eta(t))\Delta t_{\rm r} - \Gamma\eta(t)\Delta t_{\rm r} \quad (5.56)$$

$$= \eta(t)\left(1 - \frac{\Delta t_{\rm r}}{\tau_{\rm eq}}\right) + \frac{\Delta t_{\rm r}}{\tau_{\rm rec}}. \quad (5.57)$$

In the following we understand all quantities to be evaluated at time t and hence will not explicitly indicate the time dependence.

By definition the neutral fraction must satisfy $0 \leq \eta \leq 1$. Satisfying the lower bound means

$$\eta \left(1 - \frac{\Delta t_\mathrm{r}}{\tau_\mathrm{eq}}\right) + \frac{\Delta t_\mathrm{r}}{\tau_\mathrm{rec}} \geq 0, \tag{5.58}$$

which poses the conditions

$$\Delta t_\mathrm{r} \leq \frac{-\eta}{\tau_\mathrm{rec}^{-1} - \eta\tau_\mathrm{eq}^{-1}} \quad \text{for } \tau_\mathrm{rec}^{-1} - \eta\tau_\mathrm{eq}^{-1} < 0 \tag{5.59}$$

and

$$\Delta t_\mathrm{r} \geq \frac{-\eta}{\tau_\mathrm{rec}^{-1} - \eta\tau_\mathrm{eq}^{-1}} \quad \text{for } \tau_\mathrm{rec}^{-1} - \eta\tau_\mathrm{eq}^{-1} > 0 \tag{5.60}$$

on the size of the time step Δt_r. Satisfying the upper bound means, on the other hand,

$$\eta \left(1 - \frac{\Delta t_\mathrm{r}}{\tau_\mathrm{eq}}\right) + \frac{\Delta t_\mathrm{r}}{\tau_\mathrm{rec}} \leq 1, \tag{5.61}$$

which poses the conditions

$$\Delta t_\mathrm{r} \geq \frac{1-\eta}{\tau_\mathrm{rec}^{-1} - \eta\tau_\mathrm{eq}^{-1}} \quad \text{for } \tau_\mathrm{rec}^{-1} - \eta\tau_\mathrm{eq}^{-1} < 0, \tag{5.62}$$

and

$$\Delta t_\mathrm{r} \leq \frac{1-\eta}{\tau_\mathrm{rec}^{-1} - \eta\tau_\mathrm{eq}^{-1}} \quad \text{for } \tau_\mathrm{rec}^{-1} - \eta\tau_\mathrm{eq}^{-1} > 0 \tag{5.63}$$

on the size of the time step Δt_r. Let us consider the two limiting cases of fully neutral and fully ionised gas, since these are the ionisation states for which a violation of the physical bound $0 \leq \eta \leq 1$ due to an inaccurate integration is most likely. For the former, we find from Eq. 5.59 (using $\tau_\mathrm{eq} \to \tau_\mathrm{ion}$ for $\tau_\mathrm{rec} \to \infty$)

$$0 \leq \Delta t_\mathrm{r} \leq \tau_\mathrm{ion}, \tag{5.64}$$

while for the latter we find from Eq. 5.63

$$0 \leq \Delta t_\mathrm{r} \leq \tau_\mathrm{rec}. \tag{5.65}$$

In order for the neutral fraction to satisfy $0 \leq \eta \leq 1$, the time step Δt_r must be chosen such that it simultaneously satisfies the bounds Eqs. 5.64 and 5.65. Since $\tau_\mathrm{eq} \to \tau_\mathrm{ion}$ for $\tau_\mathrm{ion} \ll \tau_\mathrm{rec}$ whereas $\tau_\mathrm{eq} \to \tau_\mathrm{rec}$ for $\tau_\mathrm{rec} \ll \tau_\mathrm{ion}$ we may conveniently summarise the derived bounds by writing

$$0 \leq \Delta t_\mathrm{r} \leq f\tau_\mathrm{eq}, \tag{5.66}$$

where $f \leq 1$ is a dimensionless factor.

Finally, we note that the case of photo-ionisation equilibrium, i.e. $\eta_\mathrm{eq} = \tau_\mathrm{ion}/(\tau_\mathrm{ion} + \tau_{rec,eq})$, is formally excluded from our analysis, since then $\tau_\mathrm{rec}^{-1} - \eta\tau_\mathrm{eq}^{-1} = 0$ and Eqs. 5.59-5.62 become undefined. This simply means that in photo-ionisation equilibrium the time step can be chosen arbitrarily large[17].

[17]This statement only applies to considerations of discretization accuracy. As explained in Sec. 5.3.2, the numerically stable explicit integration of stiff equations like the photo-ionization rate equation puts an additional constraint on the size of the integration time step.

5.B CONES

5.B.1 Cone tessellation

In this section we describe the numerical implementation of the cones employed for the emission and reception of photon packets in TRAPHIC. For the emission (Sec. 4.4.2 in Chapter 4), each source particle divides its neighbourhood using a set of tessellating emission cones. The same tessellation is also employed for the reception of photon packets by gas particles (Sec. 4.4.2 in Chapter 4). In the following, we employ spherical coordinates (r, ϕ, θ), which are related to the Cartesian components (r_x, r_y, r_z) of an arbitrary vector $\mathbf{r}$ through

$$r_x = r\cos\phi\sin\theta \tag{5.67}$$
$$r_y = r\sin\phi\sin\theta \tag{5.68}$$
$$r_z = r\cos\theta. \tag{5.69}$$

In our implementation, the emission (reception) cones sample the volume around each particle isotropically. Since the surface element of the unit sphere is given by $ds = d(\cos\theta)d\phi$, this is achieved by distributing the cone boundaries[18] uniformly (i.e. on a regular lattice with indices i, j) in $(\cos\theta, \phi)$. Thus, the boundaries of cone (i, j) are described by the four arcs of constant

$$\phi_1^{ij} = i\frac{2\pi}{N_\phi}, \quad 0 \le i < N_\phi, \tag{5.70}$$
$$\phi_2^{ij} = (i+1)\frac{2\pi}{N_\phi}, \quad 0 \le i < N_\phi, \tag{5.71}$$
$$\theta_1^{ij} = \arccos(1 - 2\frac{j}{N_\theta}), \quad 0 \le j < N_\theta, \tag{5.72}$$
$$\theta_2^{ij} = \arccos(1 - 2\frac{j+1}{N_\theta}), \quad 0 \le j < N_\theta. \tag{5.73}$$

Correspondingly, we define the emission (reception) cone axes by

$$\phi^{ij} = \frac{\phi_1^{ij} + \phi_2^{ij}}{2}, \tag{5.74}$$
$$\theta^{ij} = \frac{\theta_1^{ij} + \theta_2^{ij}}{2}, \tag{5.75}$$

Note that each of the $N_\mathrm{c} = N_\phi \times N_\theta$ emission (reception) cones has the same solid angle $\Omega = 4\pi/N_\mathrm{c}$, as can be seen from integrating over the surface element of the unit sphere within the boundaries (Eqs. 5.70-5.73). We also implemented the tessellation used in Abel, Norman, & Madau (1999), which leads to cones that are more similar in shape. We could not find any systematic differences in the test problems described in Secs. 5.4.2 - 5.4.5 using either of the two types of tessellations. This is not surprising because any artefacts due to the shape of the cones will be suppressed by the random rotations of the emission (reception) cones we perform before each emission (reception). Our implementation of these rotations is described in the next section.

[18] Strictly speaking, one should distribute the cone *axes* uniformly in $(\cos\theta, \phi)$, but this implies asymmetric cones.

5.B.2 Random rotations

Recall from Sections 4.4.2 and 4.4.2 (Chapter 4) that we apply a random rotation to each cone tessellation. Consequently, each cone tessellation has a random orientation. The primary motivation for randomly rotating cones is to increase the angular sampling. Furthermore, randomly rotating the emission and reception cones leads to a reduction of artefacts arising from the particular definition we employ to construct the cone tessellation, as noted in the last section. Here we describe our numerical implementation of the random rotations.

We can think of the set of cones that comprises a particular cone tessellation as a rigid body, to which we can attach a local Cartesian coordinate system with axes $\{e'_x, e'_y, e'_z\}$. The orientation of this coordinate system with respect to the canonical Cartesian coordinate system, e.g. the simulation box axes $\{e_x, e_y, e_z\}$, is fully described by three variables, the Eulerian angles (e.g. Goldstein 1980).

Eulerian angles are defined as the three successive angles of rotations that map the axes $\{e_x, e_y, e_z\}$ onto the axes $\{e'_x, e'_y, e'_z\}$. There exist several conventions. In the zxz convention we employ here, the initial system of axes $\{e_x, e_y, e_z\}$ is first rotated counter-clockwise by an angle ϕ around the z-axis, with the resulting coordinate system labelled $\{e_\xi, e_\eta, e_\zeta\}$. Second, the coordinate system $\{e_\xi, e_\eta, e_\zeta\}$ is rotated by an angle θ counter-clockwise about the ξ-axis, leaving the new coordinate system $\{e'_\xi, e'_\eta, e'_\zeta\}$. The third and last rotation is carried out counter-clockwise by an angle ψ around the ζ'-axis, giving the desired $\{e'_x, e'_y, e'_z\}$ coordinate system.

To obtain random Eulerian angles, we note that the invariant measure μ (the "volume element") on $\mathrm{SO}(3)$, the group of proper rotations in $\mathbb{R}^3$, in the zxz Eulerian angle parametrisation reads (e.g. Miles 1965),

$$\mu(\phi, \theta, \psi) d\phi d\theta d\psi = \frac{1}{8\pi} \sin\theta d\phi d\theta d\psi. \tag{5.76}$$

Random Eulerian angles are therefore obtained by drawing random variables u_1, u_2, u_3 from a uniform distribution on the interval $[0, 1]$ and applying the usual transformation (cp. Press et al. 1992),

$$\begin{aligned} \phi &= 2\pi u_1 && (5.77)\\ \theta &= \arccos(1 - 2u_2) && (5.78)\\ \psi &= 2\pi u_3. && (5.79) \end{aligned}$$

We implement random rotations using rotation matrices, which are obtained from the random Eulerian angles. The matrix elements of a matrix R representing a rotation $\mathbf{r}' = \mathbf{R}\mathbf{r}$ associated with a given set of Eulerian angles can be readily calculated (e.g. Goldstein 1980):

$$R = \begin{pmatrix} \cos\psi\cos\phi - \cos\theta\sin\phi\sin\psi & \cos\psi\sin\phi + \cos\theta\cos\phi\sin\psi & \sin\psi\sin\theta \\ -\sin\psi\cos\phi - \cos\theta\sin\phi\cos\psi & -\sin\psi\sin\phi + \cos\theta\cos\phi\cos\psi & \cos\psi\sin\theta \\ \sin\theta\sin\phi & -\sin\theta\cos\phi & \cos\theta \end{pmatrix}. \tag{5.80}$$

In principle, random rotation matrices can be obtained directly, without drawing random Eulerian angles (e.g. Stewart 1980). We find, however, that it is faster to generate random Eulerian angles, and then calculate the corresponding rotation matrices. Moreover, storing the three Eulerian angles instead of the nine rotation matrix elements reduces the memory cost.

5.C A NEW TREATMENT OF ABSORPTIONS BY VIRTUAL PARTICLES

In this appendix we show that the treatment of virtual particles (ViPs) in the implementation of TRAPHIC that we have used to perform the simulations published in Pawlik & Schaye (2008), and that we will refer to as the old implementation, results in a temporary underestimate of the neutral fraction just behind evolving ionisation fronts in simulations that use a high angular resolution. We will show that this underestimate is absent in simulations that employ our current implementation of TRAPHIC. Moreover, in simulations that employ this new implementation, the numerical scatter in the neutral fraction is significantly reduced.

The difference between the treatments of ViPs in the old and current implementations of TRAPHIC has already been explained in Sec. 5.4. The old and current implementation only differ in the manner in which photons that have been absorbed by ViPs are distributed amongst their neighboring SPH particles. We remind the reader that this distribution of absorptions is necessary, because ViPs are temporary constructs that are just invoked to transport photons inside cones that do not contain SPH particles (see Chapter 4). Permanent information is only stored at the SPH particles in the simulation.

The number of ionising photons a ViP absorbs depends on its neutral density. As explained in Chapter 4, the computation of this number is performed in exactly the same manner as for SPH particles. The only difference between the treatment of photons absorbed by SPH particles and ViPs is that the latter distribute the absorbed photons amongst their SPH neighbors. For this distribution of absorptions one must specify the fraction of the total that is given to each of the SPH neighbors. In the old implementation of TRAPHIC this fraction was taken to be proportional to the value of the SPH kernel of the distributing ViP at the position of the SPH neighbor. In the new version this fraction is taken to be proportional to the neutral mass with which the SPH neighbor contributed to the SPH estimate of the ViP's neutral density.

The old treatment of ViPs results in an underestimate in the simulated non-equilibrium neutral fractions. Fig. 5.20 serves to demonstrate this. Its panels show the neutral and ionised fractions around a single ionising source in a homogeneous hydrogen-only medium at times $t = 30, 100$ and 500 Myr (from left to right) obtained with the old (first and third rows) and current (second and fourth rows) implementation. The setup and parameters for the simulations presented here are identical to the setup and parameters used for the $N_{\rm SPH} = 64^3$, $N_{\rm c} = 128$ simulation presented in Test 1 in Sec. 5.4.2. In addition to the neutral (grey dots) and ionised (light red dots) fractions of each particle, Fig. 5.20 shows the median neutral (black solid curves) and ionised (red solid curves) fractions in spherical bins, which are compared to the exact solution obtained with TT1D (dashed curves of the corresponding color). The error bars indicate the 68.3% confidence intervals in each bin. For each implementation we have performed simulations both with and without resampling the density field, as indicated by the presence or absence of the letter 'R' in the panel titles. Note that the right-most panels in the second and fourth row are identical (except for the bin size) to the right-most panels in the top and bottom row of Fig. 5.5 in Sec. 5.4.2.

In the simulations employing the old implementation of TRAPHIC the neutral fraction at times $t = 30$ and 100 Myr is underestimated at radii slightly smaller than the radius of the ionisation front. In the simulations that employ the current implementation this underestimate, thanks to the new manner in which the ViPs' absorptions are distributed, is no longer present. At $t = 500$ Myr, i.e. when the ionised region has (nearly) reached its equilibrium size, the underestimate is also absent in the simulations that employ the old implementation. However, at this time these simulations still exhibit an increased scatter around the median when compared to the corresponding snapshots from the simulations that employ the current implementation.

The underestimate of the neutral fraction just behind evolving ionisation fronts in simulations employing the old implementation is caused by the fact that in this implementation the distribution of the photons absorbed by ViPs does not respect the spatial distribution of the neutral gas in their surroundings. It mainly affects the neutral fraction of particles close to evolving ionisation fronts, because the number of photons absorbed and subsequently distributed by ViPs near the ionisation front is significantly larger than the number of photons that are absorbed by the SPH particles behind the ionisation front that have already reached photo-ionisation equilibrium and because the ViPs distribute the absorbed photons irrespective of the neutral mass with which the corresponding SPH particles contributed to the computation of its neutral density. The absorptions that SPH particles behind evolving ionisation fronts receive from ViPs in addition to the number of photons they have already absorbed according to their own optical depth therefore results in an overestimate of the photo-ionisation rate and hence an underestimate of the neutral fraction. Once the ionisation front becomes stationary the underestimate of the neutral fraction practically disappears, because the number of photons absorbed and distributed by ViPs in the ionisation front is consistent with the expectations from photo-ionisation equilibrium.

We did not notice the described temporary underestimate of the neutral fraction just behind non-equilibrium ionisation fronts in the simulations that we have presented in our original publication, i.e. in Pawlik & Schaye (2008), since there we only discussed profiles of the neutral fraction at $t = 500$ Myr. The reason why we limited ourselves to discussion of equilibrium results in that publication was mainly that we were at that time still lacking accurate non-equilibrium reference solutions: our one-dimensional reference radiative transfer code TT1D was still under development. The discovery of the underestimate of the neutral fraction was triggered by scatter plots of the neutral and ionised fractions like those presented in Fig. 5.20 that we have performed more recently.

5.D Power-law initial conditions for smoothed particle hydrodynamics simulations

In this appendix we describe the procedure that was used to generate the centrally peaked density field with spherically averaged profile $\rho(r) \propto r^{-1}$ employed in Test 3 in Sec. 5.4.4. We will explain more generally how to generate power-law density profiles

$$\hat{\rho}(r) \propto r^{-n}, \tag{5.81}$$

and then consider the special case $n = 1$.

The gas density at a given position is proportional to the probability of finding a gas particle at this position (assuming that the particle mass is the same for all gas particles). Arbitrary Smoothed Particle Hydrodynamics (SPH) density fields can therefore be generated using Monte Carlo methods. We have employed such a method in Sec. 5.4.5. Monte Carlo methods yield, however, particle distributions that are subject to Poisson noise. Alternative methods of generating density fields that avoid this noise are therefore often more desirable.

The uniform density fields used to initialise cosmological SPH simulations, for example, are obtained by placing particles at glass-like instead of Monte Carlo positions. Glass-like positions may be considered as regularised Monte Carlo positions. They are produced by first placing particles randomly in the simulation box and thereafter letting them freely evolve under the influence of a reversed-sign (i.e. repelling) gravitational force until they settle down into an

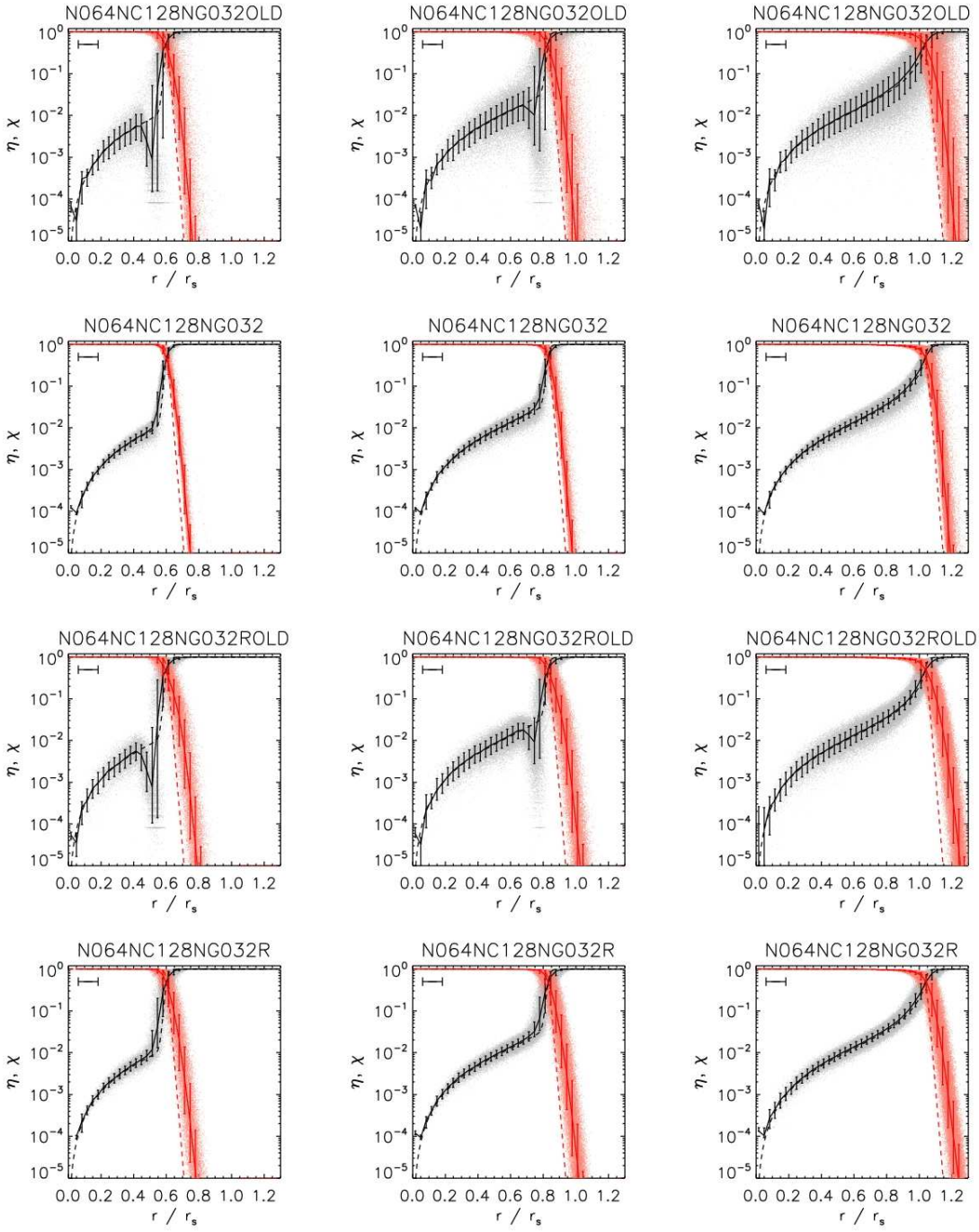

Figure 5.20: Test 1. Neutral and ionised fractions obtained in simulations with the old (first and third row) (Pawlik & Schaye 2008) and current (second and fourth row) implementations of TRAPHIC. Shown are profiles of neutral and ionised fraction at times $t = 30$ (left-hand panel), 100 (middle panel) and 500 Myr (right-hand panel), for simulations with (second and fourth row) and without (first and third row) resampling of the density field. The spatial resolution is fixed to $N_{\rm SPH} = 64^3$, $\tilde{N}_{\rm ngb} = 32$ and is indicated by the horizontal error bar in the upper left corner of each panel. The angular resolution is $N_{\rm c} = 128$. The grey (light red) points show the neutral (ionised) fraction of each SPH particle. The solid black (red) curve shows the median neutral (ionised) fraction in spherical bins and the error bars show the corresponding 68.3% confidence intervals. The dashed black (red) curves show the exact solution, obtained with our reference code TT1D. The non-equilibrium underestimate of the neutral fraction exhibited in simulations with the old implementation of TRAPHIC is absent in the simulations that employ our current implementation, thanks to a new self-consistent manner of distributing photons absorbed by ViPs. The new implementation also reduces the scatter in the ionisation balance.

equilibrium configuration (see White 1996). This regularisation leads to a significant reduction of small-scale fluctuations in the (random) inter-particle distances.

These glass-like density fields can also be used to set up centrally peaked power-law density fields of the desired form, Eq. 5.81 (Volker Springel, Claudio Dalla Vecchia, private communication). The idea is to deform the (unstructured) grid traced out by the set of uniformly distributed particles at glass-like positions such as to locally stretch the mean inter-particle distance in the radial direction. Assume that the uniform, glass-like particle distribution has density ρ_0 and express this stretching by a coordinate transformation in spherical coordinates, $(r, \theta, \phi) \rightarrow (\hat{r}, \theta, \phi)$. Mass conservation requires the new particle positions to satisfy

$$\hat{\rho}(\hat{r})\hat{r}^2 \sin\theta d\hat{r} d\theta d\phi = \rho_0 r^2 \sin\theta dr d\theta d\phi, \tag{5.82}$$

Substituting the desired density profile Eq. 5.81, the coordinate transformation reads

$$\hat{r}^{2-n} d\hat{r} \propto r^2 dr, \tag{5.83}$$

which can be easily integrated,

$$\hat{r} \propto r^{3/(3-n)}. \tag{5.84}$$

To set up the density field used in Test 3 in Sec. 5.4.3 we are interested in producing a centrally peaked density field with power-law index $n = 1$. In this case, the last expression gives $\hat{r} \propto r^{3/2}$.